Hill Shannon (Orcid ID: 0000-0002-9932-9601)
Buzulukova Natalia (Orcid ID: 0000-0002-8127-2248)
Boardsen Scott, A. (Orcid ID: 0000-0002-5240-044X)
Fok Mei-Ching, H. (Orcid ID: 0000-0001-9500-866X)

Confidential manuscript submitted to Journal of Geophysical Research: Space Physics

Local Heating of Oxygen Ions in the Presence of Magnetosonic Waves: Possible Source for the Warm Plasma Cloak?

S. Hill[1], N. Buzulukova[2,3], S. Boardsen[2,4], and M.-C. Fok[2]

[1]University of Michigan, Ann Arbor, MI, USA

[2]NASA Goddard Space Flight Center, Geospace Physics Laboratory, MD, USA

[3] Goddard Planetary Heliophysics Institute, University of Maryland, College Park, MD, USA

[4] Goddard Planetary Heliophysics Institute, University of Maryland, Baltimore, MD, USA

Corresponding author: Shannon Hill (shanhill@umich.edu)

Key Points:

- Thermal oxygen perpendicular heating is observed in the presence of magnetosonic waves near plasmaspheric density structures
- Magnetosonic waves associated with thermal oxygen heating exhibit heavy ion gyroharmonics, implying resonant interactions
- Locally heated thermal ions to 100s eV by magnetosonic waves by plasmapause provide a possible mechanism for warm plasma cloak generation

Abstract

In the energy regime between the plasmasphere (a few eVs) and the ring current (greater than 1 keV), there exists another magnetospheric particle population with energies from a few eV to a few keV, the origins of which are debated. Studies explore generation mechanisms for warm plasma energies in the inner magnetosphere through two observed phenomena: the warm plasma cloak and the oxygen torus. The relations between these two populations are unclear. Recent data reveal local heating of cold H+ and He+ ions to warm plasma energies by magnetosonic waves. In this study, we report first observations of thermal O+ heating by magnetosonic waves and link the heating to a possible formation mechanism for the warm plasma cloak. The O+ heating is observed by different plasmaspheric density profiles, including density channels. We observe that O+ heating always occurs with thermal H+ and He+ heating. We investigate the harmonic structure of the observed magnetosonic waves and find intense O+ heating is accompanied by discrete heavy ion gyroharmonics. We suggest that locally heated thermal ions to 100s eV by magnetosonic waves along the plasmapause could provide a possible mechanism for warm plasma cloak generation.

1 Introduction

Surveys completed by various spacecraft including ATS-5 and ATS-6 (DeForest and McIlwain, 1971), ISEE-1 (Shelley et al., 1978), SCATHA (Stevens and Vampola, 1978), Dynamics Explorer 1 (Roberts et al., 1987), and Polar satellites (Moore et al., 1995; Shelley et al., 1995), reveal a warm particle population (tens of eV to a few keV) that is distinct from the plasmasphere and ring current in energy and location (Chappell et al., 2008). Recent studies seek to explain the origins of the warm plasma population in the inner magnetosphere via two observed phenomena: the warm plasma cloak and the oxygen torus (e.g. Chappell, 1982; Horwitz et al., 1984 & 1986; Roberts et al., 1987; Fraser et al., 2005; Chappell et al., 2008; Nosé et al., 2015; Chappell 2015). The reported energy range and spatial distribution for the oxygen ion population in the warm plasma cloak and the oxygen torus are nearly identical. Chappell et al. (2008) identifies the energy of the O+ ions in the warm plasma cloak to be a few eV to 3 keV and Nosé et al. (2015) finds that O+ ions in the oxygen torus have thermal (1 eV - ~100 eV) and suprathermal (~100 eV – 10 keV) components. The warm plasma cloak forms a drape across the outside of the plasmasphere at MLT sectors spanning 0 MLT to 18 MLT (Figure 15 in Chappell, 2015). Chappell et al. (2008) suggests that the warm plasma cloak is populated by a stepwise acceleration mechanism for ionospheric ions of polar wind at high geomagnetic latitudes that circulates the ions across the polar cap, out towards the magnetotail, and back into the middle magnetosphere where the ions are spatially limited to outside of the plasmasphere. The oxygen torus is confined to the deep inner magnetosphere at all local times (Roberts et al., 1987), and exists in both the plasmasphere and plasma trough regions (Nosé et al., 2015).

The warm ions of the warm plasma cloak and the oxygen torus can act as a seed population for the ring current (Chappell et al., 2008; Nosé et al., 2011; Chappell, 2015) and influence the growth and behavior of waves (Fraser et al., 2005; Lee & Angelopoulos, 2014). The oxygen torus has been connected to an oxygen rich ring current and the global circulation of oxygen in the magnetosphere (Nosé et al., 2011). Increased oxygen content in the ambient plasma affects the wave dispersion in the background plasma (e.g. Summers et al., 2007) and EMIC minimum resonant energy (Kronberg et al., 2014). Yu et al. (2015) shows that increased oxygen plasma content increased O+ EMIC wave growth in particular. The effect of the warm plasma cloak on dayside (Borovsky et al., 2013) and duskside (Fuselier et al., 2016) reconnection rate has also been studied. Thus, the warm plasma cloak and oxygen torus are important mechanisms that affect the global circulation of plasma in the entire magnetosphere. Nevertheless, plasma with these intermediate energies have been understudied in comparison to other populations of the inner magnetosphere, e.g. plasmasphere, ring current and radiation belts. The current suggested generation mechanisms for the warm plasma cloak and oxygen torus involve large scale distribution of extracted ionospheric ions, or in other words, ionospheric outflow of O+ (e.g. Horwitz et al., 1986; Roberts et al., 1987; Chappell et al., 2008; Nosé et al., 2015). However, recent studies reveal the local heating of cold H+ and He+ ions to warm plasma energies by magnetosonic waves (Min et al., 2018; Yuan et al., 2018). In the present study, we present the first observations of local heating of cold O+ ions to warm plasma energies by magnetosonic waves, thus opening discussion for a modified warm plasma generation mechanism via magnetosonic waves.

Magnetosonic waves, also called equatorial noise, are nearly linearly polarized emissions with frequencies mostly between the proton gyrofrequency and the lower hybrid resonance frequency, with wave vectors nearly perpendicular to the background magnetic field (e.g. Russel et al., 1970, Boardsen et al., 2016). Observations (e.g. Perraut et al., 1982; Boardsen et al., 1992; Meredith et al., 2008; Chen et al., 2011) and theoretical studies (e.g. Horne et al., 2000; Liu et al., 2011; Gary et al., 2010; Zhou et al., 2014) suggest that energetic protons (~10s keV) with ring-like velocity distributions provide free energy to excite magnetosonic waves nearly perpendicular to the ambient magnetic field. Observations show magnetosonic waves are mostly confined to the geomagnetic equator (e.g. Gurnett, 1976; Santolík et al., 2002) and are found inside and outside the plasmapause (e.g. Perraut et al., 1982; Ma et al., 2013). While extensive studies have been performed to understand the effects of magnetosonic waves on relativistic electrons (Horne et al., 2007; Bortnik & Thorne, 2010; Li et al., 2014) and energetic protons (Xiao et al., 2014), the effects of magnetosonic waves on the cold ion plasma population are not well-understood. Magnetosonic waves are an important mechanism for energy transfer throughout the magnetosphere, thus it is important to analyze the conditions under which magnetosonic waves will heat thermal populations to higher energies.

Magnetosonic waves have long been theorized to transfer energy to cold ion populations through resonant interactions. Olsen (1981) correlated the transverse heating of a cold ion population to energies up to hundreds of eVs with equatorial noise. Horne et al. (2000) uses the HORTRAY code to suggest that magnetosonic waves could transversely heat low energy protons through cyclotron resonant absorption. Sun et al. (2017) shows through 1-D particle in cell simulations that magnetosonic waves can heat cold protons in the perpendicular direction due to higher-order resonances. Recently, observations from the Van Allen Probes show magnetosonic wave heating of low energy H+ and He+ populations. Min et al. (2018) presents observations of thermal H+ heating in the plasmaspheric trough region that corresponds with magnetosonic wave activity. Yuan et al. (2018) shows observations of cold H+ and He+ transversely heated to 100s of eV by magnetosonic waves in a plasmaspheric density cavity. Ma et al. (2019) calculates the proton bounce-averaged diffusion coefficients for magnetosonic waves during an observed thermal proton heating event and suggests that the magnetosonic wave frequency spectrum and total electron density could affect the diffusion coefficients. The effect of magnetosonic waves on the thermal oxygen population is understudied. To the best knowledge of the authors, thermal O+ ion heating corresponding with magnetosonic waves has yet to be directly observed until now.

To better understand the effect wave heating has on the origins of the warm plasma cloak and oxygen torus population, this study analyzes observations of thermal ion heating of H+, He+, and O+ by magnetosonic waves in low-density structures of the plasmasphere. The plasmaspheric boundary known as the plasmapause experiences various density profiles under different geomagnetic conditions and can develop troughs, plateaus, or other combinations of plasma enhancements and depressions (Horwitz et al., 1990; Sandel et al., 2001). The plasmapause is thought to be a preferable place for wave-particle interactions because of strong density gradients, plume formation, and the co-existence of plasmas with different characteristics, e.g. cold plasma of ionospheric origin, the ring current plasma and also energetic radiation belts (e.g. Nambu 1974; Foster et al., 1976; Chen et al., 2009; Sakaguchi et al., 2012). The various density profiles of the plasmapause offer a way to study the suggested effect (Ma et al., 2019) of total electron number density on the ability for magnetosonic waves to energize thermal ion populations.

We present the Van Allen Probes observations for events with large heating features of thermal H+, He+, and O+ that correspond with magnetosonic wave activity inside different plasmaspheric density structures. We analyze two events with the first reported observations of cold O+ ion heating in the presence of magnetosonic waves. We show that for one event, the O+ heating corresponds with high oxygen harmonics observed within the magnetosonic wave frequency spectrum and discuss different scenarios that could lead to such harmonic structure. In this study, we demonstrate that heavy ion components of the warm plasma cloak could be formed via magnetosonic waves inside density structures near the plasmapause, thus distinguishing the oxygen torus and warm plasma cloak populations and explaining why the warm plasma cloak naturally drapes around the plasmasphere.

2 Instrumentation

The Van Allen Probes consists of a pair of identical spacecrafts, Probe A and Probe B, each spinning with an ~11s period and moving through a geostationary transfer orbit (inclination ~10 degrees, apogee ~5.8 Re, perigee ~700 km, and period ~9 h) encompassing the inner magnetosphere, the ring current, and the radiation belts (Mauk et al., 2013). The Van Allen Probes' orbits present a unique opportunity to observe simultaneous wave and particle activity in the inner magnetosphere.   L4 Electric and Magnetic Field Instrument Suite and Integrated Science (EMFISIS) 64 samples/s magnetic field measurements and the L2 EMFISIS waveforms

(Kletzing et al., 2013) along with the L2 Electric Field and Waves (EFW) Instruments 32 samples/s electric field measurements were used to locate structures in the plasmaspheric density profile and analyze the electromagnetic wave activity inside them (Wygant et al., 2013). L3 spin-angle resolved and pitch-angle resolved data from the Helium, Oxygen, Proton, and Electron (HOPE) mass spectrometer (Funsten et al., 2013), which covers the particle energy range from ~1 eV to ~50 keV, was also used to analyze the behavior of the ion fluxes inside each density structure.

3 Observations of Magnetosonic Waves and O+ Heating Events

3.1 24 June 2013 05:30 UT – 6:30 UT Event

During June 24th, 2013 Probe A observes magnetosonic wave activity and corresponding ion heating within plasmaspheric density structures in the inner magnetosphere between 05:30 – 06:30 UT. Figure 1 shows the global geomagnetic indices observed between 22 UT of June 23rd, and 10 UT of June 24th. The days of June 23rd and 24th are characterized by moderately enhanced geomagnetic activity, with Kp index varying from 2 to 4, and complex auroral activity. Van Allen Probe A observations of ion heating occur after the substorm activity between 03 UT – 06 UT, as indicated by the blue rectangle. The SYM-H index reaches a minimum ~ -40 nT at the start of the event, just before 06:00 UT. The minimum in the SYM-H index suggests a link between substorm activity and the ring current injection**,** which may have caused a relative decrease in SYM-H up to ~ 20 nT, -20 nT at 02 UT to -40 nT at 06 UT. Between 5:30 UT and

6:30 UT, Probe A observed two magnetosonic wave events between 17 and 19 MLT, between L-shell of 3 and 4, between the magnetic latitudes of 3 degrees and 6 degrees.

Figure 2 shows the various wave characteristics observed by EMFISIS onboard Probe A between 5:30 UT and 6:30 UT on June 24th. Figure 2a and 2b show the electric field spectral intensity and the magnetic field spectral intensity, respectively. Figure 2c shows the wave normal angle (WNA) of the observed emissions and 2d shows the wave ellipticity (ε). The ellipticity and WNA measurements were computed using the singular value decomposition method from Santolík et al. (2003). The white sloping lines on each panel represent (from top to bottom) the lower hybrid resonance frequency and the local gyrofrequency for hydrogen. The local gyrofrequency decreases over time due to the weakening external magnetic field observed by Probe A as the spacecraft travels from L-shell 3 to L-shell 4. Between 5:38 UT and 5:52 UT and between 6:06 UT and 6:14 UT, we observe linearly polarized (ε ~ 0, seen in Figure 2d in green) emissions between the lower hybrid resonance frequency and the H+ local gyrofrequency that propagate nearly perpendicular to the ambient magnetic field (WNA ~ 90 degrees, seen in Figure 2c in red). As such we identify the emissions as magnetosonic waves. The first observed wave has a higher and more narrow frequency range than the second observed wave. The WNA and ellipticity of the first wave (shown in Figure 2c and 2d) show a small gap in wave emission around 5:46 UT. We also note that the magnetosonic waves do not decrease with the decreasing local gyrofrequencies and the decreasing lower hybrid resonance frequency. Instead, the magnetosonic wave frequencies stay constant, indicating that neither magnetosonic waves are observed in their source regions (Walker et al., 2015a).

Figure 3 shows the wave-particle characteristics observed by Probe A between 5:30 UT and 6:30 UT, which is during the same time interval of the two observed magnetosonic wave events shown in Figure 2. The vertical white bars seen in Figure 3b-h are the result of data gaps when plotting with Autoplot software. Figure 3a shows the EMFISIS electron density, determined by tracking the upper hybrid resonance frequency (Kurth et al., 2015). We use the electron density as a proxy for plasmaspheric density and determine plasmasphere boundaries and trough regions by noting sharp changes in the electron density profile (Han He et al., 2016). Between 5:30 UT and 6:30 UT, Probe A observed two density channels in the plasmaspheric density profile between 17 and 19 MLT, L-shells from 3 to 4, and near the geomagnetic equator, with magnetic latitudes ranging from 3 to 6 degrees. We identify the first density channel by the sharp change in electron density at 5:38 UT from ~500 cm^{-3} to ~250 cm^{-3} and at 5:52 UT from ~150 cm^{-3} to ~500 cm^{-3}. The second density channel is located between 6:05 UT and 6:14 UT as indicated by the sharp change in density from ~300 cm^{-3} to ~50 cm^{-3} at 6:05 UT and the sharp change in density from ~50 cm^{-3} to ~250 cm^{-3} at 6:14 UT. It is not unusual to see such density channels in the plasmasphere bulge region. IMAGE data shows evidence for complicated density channel configurations in the plasmasphere (Sandel et al., 2003). These plasmasphere inner-troughs or low-density channels are known to occur at all MLT, though most commonly between 1800 and 2400 MLT, and are identified by a sharp density decrease over 0.5 L-shell by a factor between

~2 and ~10 when compared to the density of nearby plasmasphere regions (Carpenter et al., 2000). Inside the first channel, around 5:46 UT there is a decrease in density from ~250 cm^{-3} to ~150 cm^{-3}, which corresponds well with the gap in WNA and ellipticity observations shown in Figure 2 at that time. This suggests that the plasmaspheric density has an effect on the magnetosonic wave properties, consistent with previous work (e.g. Ma et al., 2014, Yuan et al., 2017). The electric field spectral intensity is shown in Figure 3b, with the top black line indicating the lower hybrid resonance frequency and the lower black line indicating the local H+ gyrofrequency. The magnetosonic wave frequencies previously identified in Figure 2 are seen in Figure 3b and correspond exactly with the density channel boundaries. The magnetosonic wave amplitude peaks inside both plasmaspheric density channels, which is consistent with recent work showing that low-density regions in general are favorable in magnetosonic waves excitation (Yuan et al., 2017; Yuan et al., 2018). Figures 3c, 3e, and 3g show the energy-time spectrograms for omnidirectional particles as observed by HOPE for H+, He+, and O+ respectively. Inside each of the plasmaspheric density channels, we observe enhanced H+, He+, and O+ at energies <500 eV, indicating thermal ion heating corresponding with the magnetosonic wave activity. In the first density channel, enhanced H+ and O+ fluxes are also observed at higher energies (~10 keV and greater) after 5:45 UT. Throughout the second density channel, H+ and O+ fluxes are observed at energies between 7 and 9 keV and ~30 keV. These distributions are similar to the already reported ‘ring distributions’ (e.g. Meredith et al., 2008; Chen et al., 2011) of particles injected into the inner magnetosphere, most likely during recent substorm activity. The white line in Figure 3c represents the Alfvenic energy E_A, which is defined as $B^2(2\mu_0 n_e)^{-1}$ where B is the magnetic field magnitude and n_e is the electron number density. The dotted black line in Figure 3c represents the proton ring energy, E_R, defined by the energy of the peak in the phase space density (Horne et al., 2000; Chen et al., 2010, 2011). Magnetosonic wave growth instabilities are most favorable when E_A is comparable to E_R. E_A is most comparable to E_R inside the second channel, thus indicating that the density channel could host locally generated waves as well.

Figures 3d, 3f, and 3h show the pitch angle distribution for the ions within the energy bin 21-215 eV for H+ and He+, and 16-193 eV for O+. The enhanced ion flux observed in each density channel corresponds to perpendicular pitch angle distributions for all three ions. The transverse heating for all ion species begins and ends at the boundaries of the density channels and magnetosonic wave activity. The transversely heated ion flux for each species reaches up to a few 100 eVs. Ion fluxes are less intense in the second density channel, which corresponds with the differences in the spectral properties of the waves inside each channel.

Figure 4 shows the relative and absolute ion partial number densities observed by HOPE between 5:30 and 6:30 UT. Since the HOPE instrument cannot measure the core population of plasmasphere, the partial densities in this study correspond only to the warm plasma population with energies above 30 eV. Figure 4a shows the ratio of warm H+/total ion density n(H+)/n (black curve), warm He+/total ion density n(He+)/n (green), and warm O+/total ion density n(O+)/n (red). Figure 4b shows the partial number density for warm H+, (black), warm He+

(green), and warm O+ (red). The two blue rectangles show the intervals of the enhanced ion flux in the plasmaspheric density channels. In Figure 4a, we observe that the ratio of warm n(H+)/n(tot) increases inside each density channel, approaching 0.8 for the first channel and 0.7 for the second channel. In Figure 3, the HOPE energy time spectrograms show more intense ion heating in the first channel than in the second channel. Comparison of partial density signals between the first and second channels in Figure 4b shows that the more intense the heating, the higher the warm n(H+) and subsequently the higher the percentage of warm n(H+)/n. The warm He+ density signal (green) is also more clearly seen in the first channel than in the second, but it is not as strong as the warm H+ signal. The strength of the warm H+ signal indicates that the heating process is more effective for H+ ions, which is consistent with the theory of heating by magnetosonic waves (e.g. Horne et al., 2000; Sun et al., 2017). Thus, we suggest that the intense heating process acts on H+ predominantly, but also affects He+ and O+ ions.

It is important to note that the heating signal in warm O+ is not so evident in Figure 4, yet the perpendicular heating is very evident from the HOPE energy time spectrograms in Figure 3. In response, we suggest that the strength of the effect is lower for the O+, possibly because it is heavier, potentially less abundant, and not always in resonance with the magnetosonic wave. It is also important that the partial number density for warm O+ (Figure 4b) stays nearly constant, but the partial density ratio n(O+)/n (Figure 4a) varies significantly inside and outside the density channels. O+ is the predominant component (between 40% and 80%) of the warm plasma (energetic tail) of the plasmasphere between 5:30 and 5:38 UT, and of the warm plasma plume (~50%) between 5:52 and 6:06 UT (as measured by HOPE instrument).

The EMFISIS instrument samples the electric and magnetic fields at a rate of 35,000 samples/second. In waveform burst mode and waveform continuous burst mode, EMFISIS captures 0.486 second and 5.968 second waveforms, respectively, that can be used for frequency analysis (Kletzing et al., 2013). The frequency resolution of burst mode, Δf = 1/0.5 = 2 Hz, is small enough to resolve the proton harmonic structures and spectral substructures of the magnetosonic wave. The frequency resolution of continuous burst mode, Δf = 1/5.968 = 0.168 Hz, is small enough to resolve the helium and oxygen harmonic structures in addition to the proton harmonic structures.

During the June 24th event, EMFISIS captured one 0.468 second waveform at 5:49 UT inside the first density channel. Figure 5 shows magnetic field power spectral density at 5:49 UT, when we observe O+ heating in the first density channel. During the waveform capture the local proton gyrofrequency was 11.2 Hz. Figure 5a shows the power spectral density on a log scale between 0 Hz and 450 Hz with the local proton gyroharmonics shown with vertical grey lines. The frequency range of the observed magnetosonic wave is indicated with two yellow vertical bars. Figure 5b shows a linear scale of the magnetic field power spectral density of the magnetosonic wave emission between the 18th and 33rd proton gyroharmonics (shown by vertical grey lines). The spectral peaks in the power spectral density do not correspond with the local proton gyroharmonics, which further indicates that this wave was generated nonlocally (Walker et al., 2015a). It is possible that these magnetosonic waves were generated elsewhere and propagated towards the plasmasphere where they became trapped inside the density channels (Chen and Thorne, 2012), which is consistent with wave observations in Figures 2 and 3b which suggest that the magnetosonic waves are not in their source regions. Magnetosonic waves can retain their harmonic structure as determined by their source region conditions when they propagate away from the source and to the observation point (Perraut et al., 1982). Therefore, the observed harmonic structure reveals information about the magnetosonic wave source location. The frequency spacing between each spectral peak between the 18th and 26th proton gyroharmonics is smaller than the local proton gyrofrequency and the frequency spacing between each spectral peak between the 27th and 33rd proton gyroharmonics is larger than the local proton gyrofrequency. The smaller (larger) frequency spacing suggests that these magnetosonic wave emissions were generated in a region of lower (higher) magnetic field strength and subsequently propagated to their observation point (Walker et al., 2015a). The peak power spectral density between the 18th and 22nd proton gyroharmonics (between 5 e-6 nT2 Hz-1 and 7 e-6 nT2 Hz-1) is greater than the peak between 27th and 33rd proton gyroharmonics (less than 5 e-6 nT2 Hz-1). It is possible that the difference in frequency spacings and power spectral density between the 18th and 22nd proton gyroharmonics and between the 27th and 33rd proton gyroharmonics indicates a more complicated frequency spectrum due to a mixture of multiple magnetosonic waves (Perraut et al., 1982; Santolík et al., 2016). The local helium gyroharmonics are also resolved (11.2 Hz/4 = 2.8 Hz) and shown in Figure 5b with green dashed lines. The spectral peak between the 18th and 19th and the 29th and 30th proton gyroharmonics matches well with the He+ local gyroharmonics, suggesting resonance activity between the magnetosonic wave and He+. We also note the spectral peaks between the 19th and 20th, 21st and 22nd, 25th and 26th, and 27th and 28th local proton gyroharmonics are also between the He+ local gyroharmonics, which could indicate wave-particle resonance with heavier ions, i.e. oxygen.

When inside the second density channel on June 24th, EMFISIS was in waveform burst mode and captured 16 sets of 0.486 second waveforms from 6:06 UT to 6:14 UT. Figure 6 shows the time-averaged magnetic field frequency power spectra of eight 16384-point Fourier transforms centered at 6:08 UT (Figures 6a and 6b) and 6:12 UT (Figures 6c and 6d). The average local proton gyrofrequency was 7.4 Hz between 6:06 and 6:10 UT (first time interval) and 6.85 Hz between 6:10 and 6:14 UT (second time interval). The time duration of each waveform sample (1/0.5s = 2 Hz) restricts the resolution of helium and oxygen gyroharmonics, but proton harmonic structure is resolved. The dashed black lines represent the local proton gyroharmonics for each time interval. Figure 6a and Figure 6c show the power spectral density on a log scale between 0 and 350 Hz, centered around the time intervals 6:08 UT and 6:12 UT, respectively. We observe the magnetosonic wave emission in the frequency interval marked by two yellow bars (150-300 Hz) for each time. Figure 6b and Figure 6d each show the magnetosonic wave power spectral density on a linear scale for the 6:08 UT and 6:12 UT time intervals, respectively. The broadband spectrum in power spectral density over a continuous frequency range between ~150 Hz and ~300 Hz during the first interval (Figure 6a), and between ~150 Hz and ~275 Hz during the second interval (Figure 6c) indicate that the observed magnetosonic wave in the second density channel is a non-harmonic continuous emission (Tsurutani et al., 2014; Chen et al., 2016). However, for both four-minute time intervals, the frequency power spectra in Figure 6b and 6d show discrete harmonic structures that do not correspond with the local proton gyroharmonics. This is again consistent with a nonlocal generation of the magnetosonic wave. We suggest that Figure 6 shows wave-wave mixing of continuous and discrete harmonic waves. We note that the spectral peaks shown in Figure 6b and 6d are between the local proton gyroharmonics, which could again indicate resonance with heavier ions. We also note that the power spectral density centered around 6:08 UT (Figure 6a) is between 8 e-5 $nT^2 Hz^{-1}$ and 6 e-5 $nT^2 Hz^{-1}$, which is nearly double that of the power spectral density centered around 6:10 UT (Figure 6b). The decrease in power spectral density over time could suggest that the wave is transferring energy over time to the heated thermal ion population in the second density channel, further supporting resonant wave heating.

3.2 14 August 2013 11:30 – 12:30 UT Event

The second magnetosonic wave event we study is between 11:30 UT and 12:30 UT on August 14th, 2013. This is a quieter time period than the previous event and the plasmaspheric density profile has different density characteristics. During this time interval, the Van Allen Probe A observations of magnetosonic waves and ion heating are in a different spatial location than the first event, between 15 and 16 MLT. EMFISIS was in waveform continuous burst mode when

HOPE observed the heavy ion heating during the second event, which presents an opportunity for a high frequency resolution analysis of the present magnetosonic waves.

Figure 7 shows the global activity characteristics observed on August 13-14th, 2013. Near 03 UT August 14th, SYM-H reaches a minimum at around -35 nT. Substorm activity persists during ~20h of the day before the observations, reaching the highest AE index values of 600-700 nT, and indicating multiple substorm occurrences. However, in the period of interest during which we observe wave-particle activity the magnetosphere is relatively undisturbed, and experiences minimal substorm activity up to 3 hours before the wave event. These conditions contrast the more disturbed environment of June 24th event, when the heating occurs at the tail end of the substorm disturbance. Different geomagnetic conditions affect global pattern of electric field in the inner magnetosphere, and hence affect the plasmasphere dynamics.

Figure 8 is in the same format as Figure 2 for the various wave characteristics observed by EMFISIS onboard Probe A between 11:30 UT and 12:30 UT. We identify the magnetosonic wave by the linearly polarized ($\varepsilon \sim 0$) emissions (Figure 8d, green) and the large WNA (Figure 8c, red). Between 11:30 UT and 11:53 UT, the wave frequency is between 30 and 100 Hz. After 11:53 UT, the wave frequency range broadens to 30-500 Hz until about 12:02 UT when it begins to narrow to a frequency range of ~200-500 Hz by 12:20 UT. The white lines shown on each panel in Figure 8 represent the lower hybrid resonance frequency and the local gyrofrequency for hydrogen. Interestingly, while the frequency range of the magnetosonic wave changes over the time interval, it does not decrease with the local gyroharmonics. Thus, Figure 8 provides suggestive evidence that the magnetosonic wave in question was again nonlocally generated. It is important to note that magnetosonic wave activity during the relatively quiet conditions could suggest that the magnetosonic wave was generated during the substorm activity 3 hours prior to observations (Meredith et al., 2008), or that the magnetosonic wave was generated elsewhere and propagated over radial distance and magnetic local time (Ma, Li, Chen, Thorne, & Angelopoulos, 2014).

Figure 9 has the same format as Figure 3 to show the ion behavior between 11:30 UT and 12:30 UT. As shown in Figure 9a, Probe A observed a fluctuating plasmaspheric density profile after leaving the plasmasphere around 16 MLT, at L-shell 3 and between 2 and 2.5 degrees from the magnetic equator. Figure 9a shows a sharp decrease in density from >500 cm^{-3} to ~200 cm^{-3} at 11:53 UT, which indicates the spacecraft crossing the plasmapause and leaving the plasmasphere (Han He et al., 2016). Between 11:57 UT and 12:00 UT, we see an increase in the density to ~350 cm^{-3}.

The increase in density between 11:57 and 12:01 UT is short in time duration (~4 mins) and L-shell duration (<0.5 L-shell), and the electron number density is smaller compared to the main plasmasphere. We suggest that the density profile between 11:57 and 12:01 UT represents a thin and wispy erosion plume wrapped around the plasmasphere, with a region of low density between the plume and the main body of the plasmasphere. We consider the interval of low density between 11:53 UT and 11:57 UT to be a plasmaspheric density channel. The thin wrapped plume and density channel are observed by IMAGE and commonly developed under recovery conditions (Sandel et al., 2003). After 12:01 UT, the density decreases from 200 cm^{-3} to 100 cm^{-3} over sixteen minutes which is consistent with observations showing weakly enhanced density outside of the plume, despite its far distance from the plasmasphere main body (Sandel et al., 2003).

In Figure 9b, the electric field spectral density shows the identified magnetosonic wave from Figure 8. Unlike the previous case on June 24th, the density gradients on both sides of the density channel between 11:53 UT and 11:57 UT do not effectively trap the magnetosonic wave in the channel. Magnetosonic waves can propagate radially and azimuthally, but preferentially travel in the azimuthal direction (Boardsen et al., 2015) following the plasmapause density gradient which acts as a wave guide (Chen and Thorne, 2012). However, the wave guide does not have to stop the magnetosonic wave from penetrating the plasmapause (Boardsen et al., 2014). Magnetosonic waves propagate radially when scattered off inhomogeneities in the plasmasphere (Ma et al., 2014). Though ray tracing analysis is beyond the scope of the present study, we can still use observations to make inferences about wave behavior. The wave characteristics shown in Figure 8 imply nonlocal generation and subsequent inward propagation. Figure 9c shows the Alfven energy, E_R (white line), and the proton ring energy, E_R (black dashed line). Outside of the plasmasphere, between 11:53 UT and 12:16 UT, $E_R > E_A$ yet E_R and E_A are still comparable, which indicates conditions for broader frequency bandwidth wave growth (Ma, Li, Chen, Thorne, & Angelopoulos, 2014). As the wave propagates inwards, Figure 9b shows the magnetosonic wave amplitude reaches a maximum between 11:54 UT and 12:16 UT, while also broadening in frequency range. We suggest that the variations in the plasmaspheric density excite the magnetosonic wave and increase the radial direction of the wave vector, which allows the wave to penetrate the plume between 11:57 UT and 12:01 UT and continue to propagate in the density channel between 11:53 UT and 11:57 UT before penetrating the plasmapause (Boardsen et al., 2014). Between 11:30 UT and 11:53 UT, E_R is much greater than E_A inside the plasmasphere, indicating unfavorable conditions for wave growth (Ma, Li, Chen, Thorne, & Angelopoulos, 2014). We suggest that the wave propagated inwards and was excited by density variations of the plume and density channel near the plasmapause until entering the plasmasphere where the wave growth decreased. Thus, the wave amplitude and frequency range are influenced by the plasmaspheric density structures, which is consistent with previous studies (e.g. Ma et al., 2014, Yuan et al., 2018).

We also observe enhanced H+, He+, and O+ fluxes (Figures 9c, e, g) for energies <500 eV that correspond with the left-side boundary of the density channel (the plasmapause) at 11:53 UT as well as the interval of the magnetosonic wave frequency range broadening between 11:53 UT and 12:01 UT. Figures 9d, f, and h show the pitch angle distribution for H+, He+, and O+, respectively, sampled at energies 13-156 eV. We observe peak intensities of perpendicular pitch angle distributions for all three ions between 11:57 UT and 12:01 UT. Each ion experiences transverse heating to a few 100 eVs during the interval of the magnetosonic wave frequency range broadening. Starting at 12:01 UT, the energy-time spectrogram for He+ (Figure 9e) shows a decrease in fluxes for the low energy band 1-50 eV, and starting at 12:05 UT, O+ fluxes at that energy range (Figure 9g) are almost absent, or very low (below 103 s-1cm-2ster-1keV-1). We interpret the reduction of He+ heating and absence of O+ low energy fluxes as the result of the spacecraft moving away from the intense heating source. We note that, in similarity with the June 24th event, the location of the intense heating source for O+ is collocated with the low-density region in the plasmaspheric density profile.

Figure 10 has the same format as Figure 4. It shows the relative and absolute ion partial number densities observed by HOPE between 11:30 and 12:30 UT for energies 30 eV and above. Figure 10a shows the ratio of warm H+/total warm ion density n(H+)/n (black curve), warm He+/total warm ion density n(He+)/n (green), and warm O+/total warm ion density n(O+)/n (red). Figure 10b shows the partial number density for warm H+ (black), warm He+ (green), and warm O+ (red). In Figure 10a, we again observe the transition from the warm O+ rich plasmasphere between 11:30 UT and 11:53 UT to a warm H+ dominated environment at 11:53 UT. The species dependent heating is seen between 11:53 and 12:01 UT, which encompasses the density channel between 11:53 UT and 11:57 UT and the thin plume between 11:57 UT and 12:01 UT. After 12:01, there is a warm H+ dominated region, with low content of warm O+ and warm He+. Interestingly, in both the June 24 interval and the August 14 interval, the O+ heating instances coincide with elevated partial density for warm He+, as shown in Figure 10b. This is consistent with our hypothesis that the heating mechanism is species dependent and affects H+ ions first, with O+ heating only observed with both He+ and H+ heating.

During the August 14th event, EMFISIS was in waveform continuous burst mode when inside the density channel and plume and subsequently captured 9 sets of 5.968 second waveforms from 11:57 UT through 11:59 UT, where we observe enhanced O+ fluxes at energies <500 eV. The magnetosonic wave emission is observed between ~30 Hz and ~300 Hz (Figure 8). During this time, the average local proton gyrofrequency was 9.72 Hz. Figure 11a shows the time-averaged magnetic field frequency power spectra of nine Fourier transformed total magnetic field waveforms centered around 11:58 UT between 0 Hz and 300 Hz. The local proton gyroharmonics are shown in solid grey lines. Figure 11b shows the same as Figure 11a, except the power spectral density is plotted on a linear scale over the frequency range 50-100 Hz. We observe the highest power spectral density and most distinct harmonic structure for the magnetosonic emission in the 70-100 Hz frequency range. The resolution of the waveform continuous burst mode is 0.168 Hz, which is small enough to resolve the local gyroharmonics for H+. He+, and O+. The local proton gyroharmonics are shown in solid grey lines and the local helium gyroharmonics and the local oxygen gyroharmonics are shown in green and red dashed lines, respectively. The spectral peaks reach a maximum power spectral density of ~1.5 e-3 nT^2 Hz^{-1}, which is 3 orders of magnitude larger than seen in both density channels on June 24th. The spectral peaks also have distinct discrete harmonic structure in a much lower frequency range than the previous event. The larger spectral peaks (>2.5 e-4 nT^2 Hz^{-1}) do not correspond with local proton gyrofrequency, which indicates a nonlocal generation consistent with observations shown in Figures 8 and 9. The frequency spacing between the larger spectral peaks is smaller than the frequency spacing between the local proton gyroharmonics, which suggests that the emissions were generated in a region of a weaker external magnetic field. The power frequency spectrum is consistent with assumption that the magnetosonic wave was generated at a larger L-shell and propagated inward towards the plasmasphere. However, the nearly even frequency spacing between the smaller spectral peaks (< 2.5 e-4 $nT^2 Hz^{-1}$) is different from the spacing between the larger peaks, which suggests that Figure 11 shows the power spectral density for complex mixture of frequency spectra of various emissions. It is also notable that in Figure 11b, the largest spectral peaks overlap or nearly overlap with the gyroharmonics for helium and oxygen and we observe transverse heating of helium and oxygen during the same time interval. Figure 11c is the same format as Figure 11b, except over the frequency range 120-170 Hz. The power spectral density is much lower for the frequency range in Figure 11c than Figure 11b. The difference between the power spectral density values for each of the spectral peaks shown in Figure 11c is also much lower than in Figure 11b. Observations in Figure 9 show the magnetosonic wave broadening in its frequency range during this time. Unfavorable conditions for high frequency wave instabilities ($E_A < E_R$ during this time) indicate that the higher frequency component (between 100 Hz and 300 Hz) is either another magnetosonic wave guided into the region by the plasmaspheric density, or that the existing magnetosonic wave is modulated by the local conditions and is transforming from a discrete harmonic structure to a more broadband continuous structure at higher proton gyrofrequencies. We also note that many spectral peaks in Figure 11c also overlap with helium and oxygen gyroharmonics.

4 Discussion

In the previous section, we present two events with three separate instances of magnetosonic wave activity corresponding with transverse heating of thermal proton, helium, and oxygen ions. We performed harmonic analysis on EMFISIS waveform burst and waveform continuous burst mode data to resolve the ion harmonic structures in the power spectral density. We found that during instances of heavy ion heating, the fine frequency structures of the power spectral density aligned well with heavy ion harmonics. In this section, we discuss thermal heating of oxygen ions by resonant interactions with magnetosonic waves, the role of the electric field pattern in the heating process, the role of other waves for thermal ion heating, and the implications of magnetosonic wave heavy ion resonant heating in the inner magnetosphere for the generation of the warm plasma cloak and the oxygen torus.

4.1 Thermal Heating of O+ through Resonant Interactions with Magnetosonic Waves

Sun et al. (2017) shows through 1D PIC simulations that magnetosonic waves can perpendicularly energize cold protons through higher order resonances when the magnetosonic wave has a finite $k_{//}$ component. In this case, the following condition for higher order resonant interactions satisfies:

$$v_{//n,res} = \frac{(\omega - \mathrm{n}\Omega_i)}{k_{//}} \quad (1)$$

where ω is the frequency of the magnetosonic waves, $k_{//}$ is the parallel wave number, n is the orders of harmonic resonances, Ω_i is the ion gyrofrequency, and $v_{//n,res}$ is the required resonant velocity. For a small, finite $k_{//}$, and for frequencies of magnetosonic waves that are close to the harmonics of the ion gyrofrequency, the resonant velocity is reduced to a sufficiently small value, which allows for resonant interactions between magnetosonic waves and thermal ions (Horne et al., 2000; Sun et al., 2017; Yuan et al., 2018). Thus, harmonic emissions of magnetosonic waves that are close to the gyroharmonics of various ion species such as protons, helium, and oxygen should theoretically be able to transversely heat such ions at thermal energies.

Though magnetosonic waves are generated with instabilities at the local proton gyroharmonics (Balikhin et al., 2015), previous observations have shown magnetosonic waves with different types of harmonic emissions in power spectral density profiles. Through electric field observations of equatorial noise (magnetosonic waves) from IMP 6 and Hawkeye 1 satellites, Gurnett (1976) reported emissions of dominant spectral peaks at various proton gyrofrequency harmonics with minor peaks at ¼ and 1/8 the proton gyrofrequency harmonics, i.e. heavier ion harmonics. Parrot et al., 2016 reported observations of equatorial noise emissions in the ionosphere with O+ harmonics. Recent observations of magnetosonic waves with CLUSTER (Walker et al., 2016), DEMETER (Santolík et al., 2016), and the Van Allen Probes (Min et al., 2018) reveal multiple spectral peaks in between the proton gyrofrequency harmonics, which could indicate resonance with heavier ions.

The power spectral density for each magnetosonic wave analyzed in the present study shows a complex frequency spectrum indicative of multiple wave emissions. Perraut et al., (1982) provides a study of magnetosonic waves with complicated harmonic structures differing from local proton gyroharmonics, one reason for which he suggests is wave-wave coupling between multiple magnetosonic wave emissions. The wave guide provided by the density channel can direct multiple emissions to the same region. We suggest that both density channels in the first event behave as wave guides and trap nonlocally generated magnetosonic waves. The waves were generated in a region with a different magnetic field and propagated inwards while retaining their harmonic structure. Thus, the nonlocal proton gyroharmonics of the magnetosonic wave are at fractions of the local proton gyroharmonics within the density channel. In the first density channel, the frequency power spectrum obtained at 5:49 UT in Figure 5 shows spectral peaks close to or overlapping with He+ and possible O+ local gyroharmonics, satisfying equation (1) for a particular resonant thermal velocity. The harmonic spectral structures suggest that resonant interactions between the magnetosonic wave and the thermal ions in the first density channel are a reason for the observed transverse heating of thermal He+ and O+ observed in Figure 3. We suggest that the frequency power spectrum captured in the second density channel (Figure 6) shows both a discrete harmonic structure as well as a continuous structure for the magnetosonic wave. Gurnett (1976) shows a mixture of discrete and non-discrete spectra for the electric field observations of magnetosonic wave. Due to magnetosonic wave ability to propagate in radial and azimuthal directions, broader frequency spectrums such as those shown in Figure 6 and Figure 8 can result from wave power mixing from a nearby broad source region (Chen et al., 2011). We observe the discrete harmonic peaks in between the local proton gyroharmonics. Thus, we suggest that the mixture of discrete and non-discrete spectra arises from a mixture of wave frequencies from multiple nonlocal magnetosonic waves that were guided by the plasmaspheric density channel. However, Figure 3c shows that E_A is most comparable to E_R inside the second density channel, which indicates a potential region for locally generated magnetosonic waves (Chen et al., 2011). Thus, we also suggest that the nonlocally sourced wave could be mixing with a locally generated emission in the second density channel. The more intense oxygen heating in the first density channel could be explained by the discrete harmonic magnetosonic wave emissions at fractions of the proton gyroharmonics. In comparison, the less intense heating in the second channel could be explained by the discrete and non-discrete magnetosonic wave spectrum that may not be as efficient in wave-particle resonant heating.

PIC simulations and linear theory have also been used to show magnetosonic wave instabilities can form in between discrete proton harmonics (Chen et al., 2016; Min et al., 2018). Chen et al., (2016) recently showed through a study of frequency spectra of magnetosonic waves that continuous magnetosonic wave emissions result from the formation of numerous neighboring discrete peaks at fractions of the proton gyrofrequency harmonics. When the magnetosonic wave propagates with a finite $k_{//}$ component, more instabilities will form in between the proton gyroharmonics (Chen et al., 2016). The neighboring harmonics will form at fractions of the proton gyroharmonics until the frequency spectrum is continuous. The fractional proton gyroharmonics could give rise to wave-particle resonant interactions between magnetosonic waves and heavier ions.

For the case on August 14th, 2013 the frequency power spectrum shows significant difference in power spectral density across frequency range, which suggests that, like the first event, the mixture of multiple magnetosonic waves. The frequency power spectrum shows discrete peaks between $6\Omega_p$ -$10\Omega_p$ (Figure 11b) that correspond with heavy ion gyroharmonics. The discrete peaks are the result of a nonlocally generated magnetosonic wave propagating to a region with a larger magnetic field. Between $11\Omega_p$ - $29\Omega_p$ (Figure 11a), the power spectrum shows broad spectrum harmonic structure with many fine spectral peaks between the proton gyroharmonics that line up with heavy ion gyroharmonics (Figure 11c). We suggest that the frequency range between $11\Omega_p$ - $29\Omega_p$ is a good example of magnetosonic wave emissions that are not yet continuous but forming neighboring peaks in between the proton gyroharmonics. In Figure 11b and 11c, many spectral peaks overlap with the helium and oxygen gyroharmonics and are very close to the proton gyroharmonics, satisfying equation (1) for a particular resonant velocity. Thus, we expect resonant wave-particle interactions with transverse heating of H+, He+, and O+. The expected heating is consistent with observations of ion behavior in Figure 7.

For magnetosonic waves to heat ions through resonant interactions, the wave harmonics must be close to the ion gyroharmonics. We suggest three ways that magnetosonic wave harmonics could become close to the gyroharmonics of oxygen:

(1) Magnetosonic wave propagates from region of low magnetic field to high magnetic field, while retaining harmonic structure of source conditions. In regions with a high enough magnetic field, the source proton gyroharmonics become comparable to the local oxygen gyroharmonics, which allows for resonant interactions.

(2) As the magnetosonic wave propagates, harmonic instabilities form in between proton gyroharmonics as the wave harmonic structure transforms from a discrete to continuous spectrum.

(3) A mixture of multiple magnetosonic waves creates a complicated frequency spectrum that includes peaks in the power spectral density at the local oxygen gyroharmonics.

Table 1 shows the combination of the above processes for the three instances of oxygen heating presented in this study.

4.2 Role of Electric Field Pattern in Heating Process

Another important aspect for the heating of thermal ions by magnetosonic waves is the shape of the plasmasphere. Variations in global electric field pattern will modulate the plasmaspheric density, thus creating various structures, such as density channels. The substorm activity plays a dual role in the ion heating process. First, substorms serve as a source of free energy for wave instabilities, by supplying fresh injected plasma into the inner magnetosphere and forming unstable ring distributions. Secondly, substorms induce perturbations in the global convection field by creating multiple plumes and density channels that serve as waveguides.

In the present study we observe the ion heating at different MLT values, thus naturally the density structures will be different because of the prehistory of the electric field, plasmapause position, and the shape of the plume. Figure 12 shows our interpretation of the plasmasphere dynamics during the first and second event. The shapes of the plasmasphere are recreated from Sandel et al. (2003) and rotated 90 degrees with the shape of the density channel modified to better match observations for each event. The spacecraft trajectory over 5:30 UT to 6:30 UT (Figure 12a) and over 11:30 UT to 12:30 UT (Figure 12b) is plotted in red. Figure 12a shows Probe A leaving the main body of the plasmasphere, crossing over the first density channel to the plume region, entering the second density channel, and crossing into a second plume region. Figure 12b shows Probe A leaving the main body of the plasmasphere and entering a density channel, then encountering a thinly wrapped plume feature characteristic of recovery times. Figure 12 shows the density channel formation near the stagnation region, which coincides with our observations of ion heating. The detailed studies of complex interplay between stagnation region, substorm injections and heating by magnetosonic waves will remain the subject for the future work.

4.3 Role of other waves for the observed thermal heating

Besides magnetosonic waves, EMIC waves are able to heat ambient cold plasma through resonant interactions (e.g. Anderson & Fuselier, 1994; Horne & Thorne, 1997; Thorne & Horne 1993). EMIC waves occur in three distinct wave frequency bands: the H+ band located between the local hydrogen gyrofrequency and the local helium gyrofrequency, the He+ band located between the local helium gyrofrequency and the local oxygen gyrofrequency, and the O+ band located below the local oxygen gyrofrequency (Horne and Thorne, 1994). Although it is thought that EMIC waves will preferentially grow in the high-density regions and not inside low-density channels (Thorne & Horne, 1997; de Soria-Santacruz et al., 2013), we analyze both events in this study for low-frequency magnetic field fluctuations to exclude EMIC wave effects.

We implement an 8192-point FFT on the B_y magnetic field component in GSM coordinates of the EMFISIS high resolution magnetometer data recorded at 64 samples/s. We use a Hanning window with 7/8 overlap. Figure 13 shows the results of the Fourier transform over three intervals. The two sloping white lines in each panel represent to the local helium (top) and oxygen (bottom) gyrofrequencies during each interval. The first two intervals (Figures 13a and 13b) correspond to the two considered cases of O+ heating shown in the present study. The O+ heating time intervals are marked by rectangular shapes. The third interval is taken from Yu et al., (2015), which reports EMIC wave activity in the He+ and O+ bands between 17:30 UT and 17:50 UT and thus serves as a baseline for EMIC waves identification. The noise level over the 0.001-10 Hz band observed by EMFISIS does not exceed 0.01 nT^2Hz^{-1} (Kletzing et al., 2013). For the two considered intervals of O+ heating (Figures 13a and 13b), low-frequency fluctuations are weak and of the order of noise all the time. Thus, the signals can be considered artifacts of the instrumentation, not EMIC waves.

However, it is interesting to note the slight increase in magnetic field wave power (~1e-2 nT^2Hz^{-1}) adjacent to the heating intervals in Figure 13b. The low intensity low frequency fluctuations are distinctly different in characteristic than EMIC waves observed in the literature. The wave power for EMIC waves typically peaks 1 to 3 orders of magnitude higher than the low intensity low frequency fluctuations observed in Figure 13b (e.g. Wang et al., 2015; Cho et al., 2016; Blum et al., 2017; Remya et al., 2019), as shown in Figure 13c. This is important because recent work calculates the diffusion coefficients for low energy oxygen ions due to heating by EMIC waves with greater wave amplitudes than what we observe in Figure 13b (Ma et al., 2019). The signals in Figure 13b are below the local oxygen gyrofrequency, which would make the emission an O+ band EMIC wave. However, O+ EMIC waves, like all EMIC waves, occur in discrete bands of emission like shown in Figure 13c, rather than randomly clustered emissions like shown in 13a and 13b (Yu et al., 2015; Usanova et al., 2016). The low wave power and lack of discrete emission bands lead us to conclude that the low frequency fluctuations in Figure 13b are not EMIC waves and most likely instrumentation artifacts.

4.4 Implications of thermal O+ transverse heating for the formation of the warm plasma cloak and oxygen torus

It has been previously shown that magnetosonic waves can transversely heat H+, and in some cases He+, to warm cloak energies (Min et al., 2018; Yuan et al., 2018). Our study presents the first observations of magnetosonic wave resonant heating with O+. We have shown that magnetosonic waves can locally interact with thermal O+ and heat these ions to warm plasma cloak energies. Recent statistical work on the location of warm plasma in the inner-magnetosphere finds that warm oxygen dominates in the vicinity of the plasmapause, the location where we observe both magnetosonic wave oxygen heating events (Jahn et al., 2017). Previous work suggests the similarity of energy range and location for both the warm plasma cloak and the oxygen torus, with the major difference that the warm plasma cloak drapes around the outside of the plasmapause and the oxygen torus is found both inside and outside of the plasmapause (Chappell 2008; Nosé et al., 2015). Our findings allow us to explore relations between these two populations.

In one potential scenario for oxygen torus formation, O+ ions are extracted from the ionosphere in the cusp region and moved to the nightside under the convection field. Lighter ions are transported further down to the tail while oxygen ions accumulate in the inner-magnetosphere. Within a few hours after the start of a storm, there is an area with enhanced O+ density outside the plasmasphere (Roberts et al., 1987). However, recent work observes thermal oxygen mass loading into the plasmasphere before the recovery phase and suggests that the oxygen torus is formed during the initial and main phases of the geomagnetic storm and thus when the plasmasphere expands during the storm recovery phase, the oxygen torus is found inside and draped outside the plasmapause (Nosé et al., 2015).

It is important to note that HOPE instrument has lower limit of energy of a few eV and HOPE standard products from CDAWeb calculate ion partial densities and composition starting from ~ 30 eV. Therefore, all our plots of the partial plasma density and composition are missing the core of the plasmaspheric population. This is clearly seen by comparison of EMFISIS density with HOPE partial density. We observe that during each event presented in this study, the HOPE partial density data for ions >30 eV show that warm oxygen ions prevail inside the plasmasphere when compared to warm H+ and He+, and that the ion heating events inside the plasmaspheric low-density regions mark the transition between the warm oxygen-dominated energetic tail of plasmasphere (starting from 30 eV) to the warm proton-dominated regime. The observations in Figure 4 of the warm O+ density in the plasmasphere and plume are consistent with those in the literature describing the oxygen torus (Nosé et al., 2011; Nosé et al., 2015). We also note that calculation of average mass density in the inner magnetosphere involves a sophisticated method called 'magnetoseismology', and not a focus of this paper. It is tempting however to connect increased partial density of O+ inside plasmasphere with mass-load by cold O+, and therefore with oxygen torus, and this could be a subject for a future work. We also observe a different warm plasma O+ population that is locally generated by resonant interactions with magnetosonic waves in density channel structures along the plasmapause, but in this regime there is still H+ dominance, that is, magnetosonic waves preferably heat lighter ions. Therefore, we observe two different patterns for oxygen ions: colder and denser population inside the plasmasphere, and lower density but heated population in the channels, and suggest that the sources for the warm plasma cloak and the warm ions of the oxygen torus are likely different for the considered events.

The relative significance of the contribution of the locally heated ions in the inner magnetosphere (including H+ and heavy ions He+ and O+) in comparison to the contribution of the ionospheric source to the warm plasma cloak remain the subject for future work. We note that the original studies of the warm plasma cloak (e.g. Chappell et al., 2008) suggest a particular formation mechanism, e.g. an ionospheric source with the subsequent transport from the tail and mostly field-aligned distributions, and thus the connection between the transversely heated ions and the field-aligned ionospheric outflow is not immediately apparent. Recent observational, theoretical, and computational studies show that there is a perpendicular heating of particles to the energies of the warm cloak by magnetosonic waves in the pre-equatorial inner magnetosphere; however, the link between the heating process and the formation of the warm plasma cloak has not been explored. Our study demonstrates for the first time the heating of thermal oxygen by magnetosonic waves. It is very important to understand the role of the locally heated perpendicular population to the field-aligned plasma cloak and to explore local heating by waves as a possible process for warm plasma cloak formation.

The robustness of the magnetosonic wave heating mechanism to create warm oxygen plasma must be considered when comparing relative contributions of the locally heated oxygen and the ionospheric outflow to the warm plasma cloak. Calculation of wave diffusion coefficients for magnetosonic waves and thermal ions, including oxygen is necessary to understand the effects of the magnetosonic wave heating mechanism on the warm plasma cloak, and thus subject for future study. Nosé et al., (2015) simulates the convective drift of transverse thermal oxygen ions and finds that the ions are able to drift to the midnight-dawn sector, which suggests that the oxygen ions in the present study that are transversely heated via magnetosonic waves can be observed in the same locations as the field-aligned warm plasma cloak. We present two cases of

O+, He+, and H+ heating of magnetosonic waves to warm plasma cloak energies. More case studies and statistical analysis are needed to understand how a warm plasma population transversely heated via magnetosonic waves contributes to the warm plasma cloak and the magnetosphere.

5 Conclusions

In summary, we use the Van Allen Probes to study the resonant interactions between magnetosonic waves and thermal ions including oxygen in the vicinity of various plasmaspheric density structures. We propose the following conclusions:

1. Magnetosonic waves are able to transversely heat thermal oxygen populations to 100s eV through resonant interactions by satisfying the resonant condition $v_{//n,res} = \frac{(\omega - \mathrm{n}\Omega_i)}{k_{//}}$ for magnetosonic wave oxygen harmonics, as shown through our frequency spectra analysis and simultaneous HOPE particle fluxes.

2. Magnetosonic wave heavy ion harmonics form under certain conditions. Heavy ion harmonics can result when a magnetosonic wave generates under small proton gyrofrequency local conditions and then propagates to a trapping region in a high magnetic field environment. The nonlocally generated harmonic structure can then match the local heavy gyroharmonics in the trapped region. Wave-wave coupling during wave mixing can also produce complicated frequency spectra that include oxygen harmonics. Heavy ion harmonics can also be generated during wave propagation as the wave structure transforms from harmonic to continuous.

3. Magnetosonic wave heating is most likely species dependent, affecting first H+, then He+, then finally O+.

4. Locally heated thermal ions to 100s eV by magnetosonic waves along the plasmapause provide a possible generation mechanism for warm plasma cloak population.

Acknowledgments

S. Hill acknowledges NASA Goddard Space Flight Center internship program for funding and support during the summer 2019. For N. Buzulukova, this work has been partially supported by NASA grant 80NSSC19K0085. The authors also thank L. Blum for her assistance in plotting and wave identification. Figures 3, 4, 9, 10, and 13 are generated with the help of Autoplot software, http://www.autoplot.org. Geomagnetic indices plots (Figures 1 and 7) are taken from World Data Center for Geomagnetism, Kyoto, http://wdc.kugi.kyoto-u.ac.jp/. Processing and analysis of the HOPE data was supported by Energetic Particle, Composition, and Thermal Plasma (RBSP-ECT) investigation funded under NASA's Prime contract no. NAS5-01072. All RBSP-ECT data are publicly available at the Web site http://www.RBSP-ect.lanl.gov/. The work by the EFW team was conducted under JHU/APL contract 922613 (RBSP-EFW). The RBSP-EFW data can be found at http://www.space.umn.edu/rbspefw-data/. The RBSP-EMFISIS data used in this paper can be found at https://emfisis.physics.uiowa.edu/Flight/.

References

Anderson, B. J., & Fuselier, S. A. (1994) Response of thermal ions to electromagnetic ion cyclotron waves, *Journal of Geophysical Research: Space Physics*, 99, A10, 19413-19425. https://doi.org/10.1029/94JA01235

Balikhin, M., Shprits, Y., Walker, S. *et al.* Observations of discrete harmonics emerging from equatorial noise. *Nat Commun* 6, 7703 (2015) doi:10.1038/ncomms8703

Blum, L. W., J. W. Bonnell, O. Agapitov, K. Paulson, and C. Kletzing (2017), EMIC wave scale size in the inner magnetosphere: Observations from the dual Van Allen Probes, Geophys. Res. Lett., 44, 1227–1233, doi:10.1002/2016GL072316.

Boardsen, S.A., Gallagher, D.L., Gurnett, D.A., Peterson, W.K., & Green, J.L. (1992) Funnel-shaped, low-frequency equatorial waves. *Journal of Geophysical Research: Space Physics*, 97, A10, 14967-14976. https://doi.org/10.1029/92JA00827

Boardsen, S. A., G. B. Hospodarsky, C. A. Kletzing, R. F. Pfaff, W. S. Kurth, J. R. Wygant, and E. A. MacDonald (2014), Van Allen Probe observations of periodic rising frequencies of the fast magnetosonic mode, Geophys. Res. Lett., 41, 8161–8168, doi:10.1002/ 2014GL062020.

Boardsen, S. A., Hospodarsky, G. B., Kletzing, C. A., Santolík, O., Wygant, J. R., MacDonald, E., Pfaff Jr., R. F., Kurth, W. S, & Khazanov, G. V. (2015) Survey of the high resolution frequency structure of the fast magnetosonic mode and proton energy diffusion associated with these waves, SM51F-06 presented at 2015 Fall Meeting, AGU, San Francisco, Calif., 14-18 Dec.

Boardsen, S. A., et al. (2016), Survey of the frequency dependent latitudinal distribution of the fast magnetosonic wave mode from Van Allen Probes Electric and Magnetic Field Instrument and Integrated Science waveform receiver plasma wave analysis, *Journal of Geophysical Research: Space Physics*, 121, 2902–2921. https://doi.org/10.1002/2015JA021844

Borovsky, J.E., Denton, M. H., Denton, R.E., Jordanova, V.K., & Krall, J. (2013) Estimating the effects of ionospheric plasma on solar wind/magnetosphere coupling via mass loading of dayside reconnection: Ion-plasma-sheet oxygen, plasmaspheric drainage plumes, and the plasma cloak. *Journal of Geophysical Research: Space Physics*, 118, 5695–5719. https://doi.org/10.1002/jgra.50527

Bortnik, J., & Thorne, R.M. (2010) Transit time scattering of energetic electrons due to equatorially confined magnetosonic waves. *Journal of Geophysical Research: Space Physics*, 115, A07213. https://doi.org/10.1029/2010JA015283

Carpenter, D. L., Anderson, R. R., Calvert, W., Moldwin, M. B. (2000) CRRES observations of density cavities inside the plasmasphere, Journal of Geophysical Research, Vol. 105, No. A10, Pages 23,323-23,338

Chappell, C. R. (1982) Initial observations of thermal plasma composition and energetics from Dynamics Explorer-1. *Geophysical Research Letters*, 9(9), 929-932. https://doi.org/10.1029/GL009i009p00929

Chappell, C. R., Huddleston, M. M., Moore, T. E., Giles, B. L., & Delcourt, D. C. (2008) Observations of the warm plasma cloak and an explanation of its formation in the magnetosphere. *Journal of Geophysical Research: Space Physics*, 113, A09206. https://doi.org/10.1029/2007JA012945.

Chappell, C.R. (2015) Space Sci Rev, 192, 5, https://doi.org/10.1007/s11214-015-0168-5

Chen, L., and R. M. Thorne (2012), Perpendicular propagation of magnetosonic waves, Geophys. Res. Lett., 39, L14102, doi:10.1029/ 2012GL052485.

Chen, L., R. M. Thorne, and R. B. Horne (2009), Simulation of EMIC wave excitation in a model magnetosphere including structured high-density plumes, J. Geophys. Res., 114, A07221, doi:10.1029/2009JA014204.

Chen, L., Thorne, R. M., Jordanova, V. K., R. B. Horne (2010) Global simulation of magnetosonic wave instability in the storm time magnetosphere, *Journal of Geophysical Research: Space Physics*, **115**, A11, https://doi.org/10.1029/2010JA015707

Chen, L., R. M. Thorne, V. K. Jordanova, M. F. Thomsen, and R. B. Horne (2011), Magnetosonic wave instability analysis for proton ring distributions observed by the LANL magnetospheric plasma analyzer, *Journal of Geophysical Research: Space Physics,* 116, A03223, https://doi.org/10.1029/2010JA016068

Chen, L., J. Sun, Q. Lu, X. Gao,Z. Xia, & Z. Zhima (2016),Generation of magnetosonic waves over a continuous spectrum, J *Journal of Geophysical Research: Space Physics*, 121, 1137 1147,doi:10.1002/2015JA022089

Cho, J.-H., D.-Y. Lee, S.-J. Noh, D.-K. Shin,J. Hwang, K.-C. Kim, J. J. Lee, C. R. Choi, S. Thaller, and R. Skoug (2016), Van Allen Probes observations of electromagnetic ion cyclotron waves triggered by enhanced solar wind dynamic pressure, J. Geophys. Res. Space Physics,121,9771–9793, doi:10.1002/2016JA022841.

DeForest, S. E., & C. E. McIlwain (1971), Plasma clouds in the magnetosphere, *Journal of Geophysical Research: Space Physics, 76, 3587,* doi:10.1029/JA076i016p03587.

de Soria-Santacruz, M., M. Spasojevic, & L. Chen (2013), EMIC waves growth and guiding in the presence of cold plasma density irregularities, Geophys. Res. Lett., 40, 1940–1944, doi:10.1002/grl.50484.

Fraser, B. J., Horwitz, J. L., Slavin, J. A., Dent, Z. C., & Mann, I. R. (2005) Heavy ion mass loading of the geomagnetic field near the plasmapause and ULF wave implications. *Geophysical Research Letters,* ***32***, 4, https://doi.org/10.1029/2004GL021315

Foster, J. C., Rosenberg, T. J., L. J. Lanzerotti (1976) Magnetospheric conditions at the time of enhanced wave-particle interactions near the plasmapause. *J. Geophys. Res., 81, 13, 2175-2182* https://doi.org/10.1029/JA081i013p02175

Funsten, H. O., Skoug, R. M., Guthrie, A. A., MacDonald, E. A., Baldonado, J. R., Harper, R. W., ... Chen, J. (2013). Helium, Oxygen, Proton, and Electron (HOPE) Mass Spectrometer for the Radiation Belt Storm Probes mission. *Space Science Reviews*, *179*, 423–484. https://doi.org/10.1007/s11214-013-9968-7

Fuselier, S. A., et al. (2016), Magnetospheric ion influence on magnetic reconnection at the duskside magnetopause, Geophys. Res. Lett., 43, 1435–1442, doi:10.1002/2015GL067358.

Gary, S. P., Liu, K., Winske, D., & Denton, R. E. (2010). Ion Bernstein instability in the terrestrial magnetosphere: Linear dispersion theory. *Journal of Geophysical Research*, 115, A12209. https://doi.org/10.1029/2010JA015965

Gurnett, Donald A. (1976) Plasma wave interactions with energetic ions near the magnetic equator. *Journal of Geophysical Research: Space Physics*, **81**, 16, 2765-2770. https://doi.org/10.1029/JA081i016p02765

Horne, R.B., R.M. Thorne (1997) Wave heating of He + by electromagnetic ion cyclotron waves in the magnetosphere Heating near the H+-He+ bi-ion resonance frequency, *Journal of Geophysical Research*, **107**, A6, 11457-11471

Horne, R.B., Wheeler, G.V., & Alleyne, H.S.C.K. (2000). Proton and electron heating by radially propagating fast magnetosonic waves. *Journal of Geophysical Research*, **105**, 27, 597-27, 610. https://doi.org/10.1029/2000JA000018

Horne, R.B., Thorne, R.M., Glauert, S.A., Meredith, N.P., Pokhotelov, D., Santolík, O. (2007) Electron acceleration in the Van Allen radiation belts by fast magnetosonic waves. *Geophysical Research Letters*, **34**, 17, https://doi.org/10.1029/2007GL030267

Horwitz, J. L., R. H. Comfort, and C. R. Chappell (1984), Thermal ion composition measurements of the formation of the new outer plasmasphere and double plasmapause during storm recovery phase, Geophys. Res. Lett., 11, 701–704, doi:10.1029/GL011i008p00701.

Horwitz, J. L., Brace, L. H., Comfort, R. H., Chappell, C. R. (1986) Dual-spacecraft measurements of plasmasphere-ionosphere coupling. *Journal of Geophysical Research: Space Physics*, **91**, A10, 11203-11216. https://doi.org/10.1029/JA091iA10p11203

Horwitz, J. L., Comfort, R. H., Chappell, C. R. (1990) A statistical characterization of plasmasphere density structure and boundary locations. *Journal of Geophysical Research: Space Physics*, **95**, A6, 7937-7947. https://doi.org/10.1029/JA095iA06p07937

Jahn, J.-M., Goldstein, J., Reeves, G. D., Fernandes, P. A., Skoug, R. M., Larsen, B. A., & Spence, H. E. (2017). The warm plasma composition in the inner magnetosphere during 2012–2015. *Journal of Geophysical Research: Space Physics*, **122**, 11,018–11,043. https://doi.org/10.1002/2017JA024183

Kletzing, C. A., Kurth, W. S., Acuna, M., MacDowall, R. J., Torbert, R. B., Averkamp, T.,...Tyler, J. (2013). The Electric and Magnetic Field Instrument Suite and Integrated Science (EMFISIS) on RBSP. *Space Science Reviews, 179*, 127-181. https://doi.org/10.1007/s11214-013-993-6

Kronberg, E.A., Ashour-Abdalla, M., Dandouras, I. et al. (2014) *Space Science Review*, 184(1-4), 173–235. https://doi.org/10.1007/s11214-014-0104-0

Kurth, W. S., S. De Pascuale, J. B. Faden,C. A. Kletzing, G. B. Hospodarsky,S. Thaller, and J. R. Wygant (2015),Electron densities inferred from plasmawave spectra obtained by the Waves instrument on Van Allen Probes, *Journal of Geophysical Research: Space Physics*,120,904–914, doi:10.1002/2014JA020857

Lee, J. H. & V. Angelopoulos (2014) On the presence and properties of cold ions near Earth's equatorial magnetosphere. *Journal of Geophysical Research: Space Physics*, **119**, 3, 1749-1770, https://doi.org/10.1002/2013JA019305

Li, J., et al. (2014), Interactions between magnetosonic waves and radiation belt electrons: Comparisons of quasi-linear calculations with test particle simulations, Geophys. Res. Lett., 41, 4828–4834, doi:10.1002/2014GL060461.

Liu, K., Gary, S. P., & Winske, D. (2011). Excitation of magnetosonic waves in the terrestrial magnetosphere: Particle-in-cell simulations. *Journal of Geophysical Research*, 116, A07212. https://doi.org/10.1029/2010JA016372

Ma, Q., Li, W., Thorne, R.M., Angelopoulos, Vassilis (2013) Global distribution of equatorial magnetosonic waves observed by THEMIS. *Geophysical Research Letters*, **40**, 10, 1895-1901. https://doi.org/10.1002/grl.50434

Ma, Q., Li, W., Chen, L., Thorne, R. M., & Angelopoulos, V. (2014). Magnetosonic wave excitation by ion ring distributions in the Earth's inner magnetosphere. *Journal of Geophysical Research: Space Physics*, 119, 844–852. https://doi.org/10.1002/2013JA019591

Ma, Q., W. Li, L. Chen, R. M. Thorne, C. A. Kletzing, W. S. Kurth, G. B. Hospodarsky, G. D. Reeves, M. G. Henderson, and H. E. Spence (2014), The trapping of equatorial magnetosonic waves in the Earth's outer plasmasphere, *Geophys. Res. Lett., 41, 6307–6313,* doi:10.1002/2014GL061414.

Ma, Q., Li, W., Yue, C., Thorne, R. M., Bortnik, J., Kletzing, C. A., et al. (2019). Ion heating by electromagnetic ion cyclotron waves and magnetosonic waves in the Earth's inner magnetosphere. *Geophysical Research Letters*, 46. https://doi.org/10.1029/2019GL083513

Mauk, B.H., Fox, N.J., Kanekal, S.G. et al. Space Sci Rev (2013) 179: 3. https://doi.org/10.1007/s11214-012-9908-y

Min, K., Liu, K., Wang, X., Chen, L.,& Denton, R. E. (2018). Fast magnetosonic waves observed by Van Allen Probes: Testing local wave excitation mechanism. *Journal of Geophysical Research: Space Physics*,123, 497–512. https://doi.org/10.1002/2017JA024867

Meredith, N. P., Horne, R. B., & Anderson, R. R. (2008). Survey of magnetosonic waves and proton ring distributions in the Earth's inner magnetosphere. *Journal of Geophysical Research*, 113, A06213. https://doi.org/10.1029/2007JA012975

Moore, T. E., et al. (1995), The thermal ion dynamics experiment and plasma source instrument, Space Sci. Rev., 71, 409, doi:10.1007/ BF00751337.

Nambu, M. Space Sci Rev (1974) 16: 427. https://doi.org/10.1007/BF00171567

Nosé, M., K. Takahashi, R. R. Anderson, and H. J. Singer (2011), Oxygen torus in the deep inner magnetosphere and its contribution to recurrent process of O+-rich ring current formation, J. Geophys. Res., 116, A10224, doi:10.1029/2011JA016651.

Nosé, M., et al. (2015), Formation of the oxygen torus in the inner magnetosphere: Van Allen Probes observations, *Journal of Geophysical Research: Space Physics*,, 120, 1182–1196, doi:10.1002/2014JA020593

Olsen, R. C. (1981) Equatorially trapped plasma populations. *J. Geophys. Res.*, 86, A13, 11235–11245. https://doi.org/10.1029/JA086iA13p11235

Parrot, M., F. Němec, O. Santolík, andN. Cornilleau-Wehrlin (2016), Equatorial noise emissions with a quasiperiodic modulation observed by DEMETER at harmonics of the O+ ion gyrofrequency, *Journal of Geophysical Research: Space Physics*,,121,10,289–10,302, doi:10.1002/2016JA022989.

Perraut, S., Roux, A., Robert, P., Gendrin, R., Sauvaud, J.-A., Bosqued, J.-M., ... Korth, A. (1982). A systematic study of ULF waves above F/H plus/ from GEOS 1 and 2 measurements and their relationships with proton ring distributions. Journal of Geophysical Research, 87, 6219–6236. https://doi.org/10.1029/JA087iA08p06219

Remya, B., Sibeck, D. G., Halford, A. J., Murphy, K. R., Reeves, G. D., Singer, H. J., Wygant, J. R., Farinas Perez, G., Thaller, S.A., Reddy, R. V. (2019) Statistical distribution of EMIC waves and dependence on substorm injections, URSI AP-RASC 2019, New Delhi, India

Roberts, W. T., Jr., J. L. Horwitz, R. H. Comfort, C. R. Chappell, J. H. Waite Jr., and J. L. Green (1987), Heavy ion density enhancements in the outer plasmasphere, J. Geophys. Res., 92, 13,499–13,512, doi:10.1029/JA092iA12p13499.

Russell, C.T., Holzer, R.E., Smith, E.J. (1970) OGO 3 observations of ELF noise in the magnetosphere: 2. The nature of the equatorial noise. *Journal of Geophysical Research*, **75**, 4, 755-768. https://doi.org/10.1029/JA075i004p00755

Sakaguchi, K., Y. Miyoshi, E. Spanswick, E. Donovan, I. R. Mann, V. Jordanova, K. Shiokawa, M. Connors, and J. C.Green (2012), Visualization of ion cyclotron wave and particle interactions in the inner magnetosphere via THEMIS-ASI observations, J. Geophys. Res.,117, A10204, doi:10.1029/2012JA018180.

Sandel, B. R., King, R. A., Forrester, W. T., Gallagher, D. L., Broadfoot, A. L., C. C. Curtis (2001) Initial results from the IMAGE Extreme Ultraviolet Imager, *Geophys. Res. Lett.*, 28, 8, 1439-1442, https://doi.org/10.1029/2001GL012885

Sandel, B. R., Goldstein, J. D., Gallagher, L., Spasojevic, M (2003) Extreme Ultraviolet Imager Observations of The Structure And Dynamics Of The Plasmasphere, Space Science Reviews 109: 25–46, 2003.

Santolík, O., Pickett, J.S., Gurnett, D.A., Maksimovic, M., Cornilleau-Wehrlin, N. (2002). Spatiotemporal variability and propagation of equatorial noise observed by Cluster. *Journal of Geophysical Research: Space Physics*, **107**, A12, SMP 43-1 SMP 43-8. https://doi.org/10.1029/2001JA009159

Santolík, O., Parrot, M., F. Lefeuvre (2003) Singular value decomposition methods for wave propagation analysis, *Radio Science*, **38**, 1, 1010, doi:10.1029/2000RS002523

Santolík, O., Parrot, M., & Němec, F. (2016). Propagation of equatorial noise to low altitudes: Decoupling from the magnetosonic mode. Geophysical Research Letters, 43, 6694–6704. https://doi.org/10.1002/2016GL069582

Shelley, E. G., R. D. Sharp, R. G. Johnson, J. Geiss, P. Eberhardt, H. Balsiger, G. Haerendel, and H. Rosenbauer (1978), Plasma composition experiment on ISEE-A, IEEE Trans. Geosci. Electron., 16, 266, doi:10.1109/TGE.1978.294560.

Shelley, E. G., et al. (1995), The toroidal imaging mass-angle spectrograph (TIMAS) for the polar mission, Space Sci. Rev., 71, 497, doi:10.1007/BF00751339.

Stevens, J. R., , and A. L. Vampola (Eds.) (1978), Description of the Space Test Program P78-2 Spacecraft and Payloads, Rep. SAMSO TR-78-24, U.S. Air Force Space and Missile Syst., Los Angeles Air Force Sta., Los Angeles, Calif.

Summers, D., Ni, B., Meredith, N.P. (2007) Timescales for radiation belt electron acceleration and loss due to resonant wave particle interactions: 1. Theory. J. Geophys. Res. 112(A4), A04206. doi: 10.1029/2006JA011801

Sun, J., Gao, X., Lu, Q., Chen, L., Liu, X., Wang, X.,… Wang, S. (2017). Spectral properties and associated plasma energization by magnetosonic waves in the Earth's magnetosphere: Particle-in-cell simulations. *Journal of Geophysical Research: Space Physics, 112, 5377-5390*. https://doi.org/10.1002/2017JA024027

Thorne, R. M., R. B. Horne (1993) Cyclotron absorption of ion-cyclotron waves at the bi-ion frequency, *Geophys. Res. Lett., 20, 4, 317-320*

Tsurutani, B. T., B. J. Falkowski, J. S. Pickett, O. P. Verkhoglyadova, O. Santolik, and G. S. Lakhina (2014), Extremely intense ELF magnetosonic_waves: A survey of polar observations, *Journal of Geophysical Research: Space Physics*, 119, 964–977, doi:10.1002/2013JA019284.

Usanova, M. E., D. M. Malaspina,A. N. Jaynes, R. J. Bruder, I. R. Mann,J. R. Wygant, and R. E. Ergun (2016),Van Allen Probes observations ofoxygen cyclotron harmonic waves in the inner magnetosphere,Geophys. Res.Lett.,43, 8827–8834, doi:10.1002/2016GL070233.

Walker, S. N., M. A. Balikhin,D. R. Shklyar, K. H. Yearby, P. Canu,C. M. Carr, and I. Dandouras (2015a),Experimental determination of the dispersion relation of magnetosonic waves, *Journal of Geophysical Research: Space Physics*,120, 9632–9650, doi:10.1002/2015JA021746.

Walker, S. N., A. G. Demekhov, S. A. Boardsen, N. Y. Ganushkina, D. G. Sibeck, and M. A. Balikhin (2016), Cluster observations of non– time continuous magnetosonic waves, *Journal of Geophysical Research: Space Physics*, 121, 9701–9716, doi:10.1002/2016JA023287.

Wang, D., et al. (2015), Statistical characteristics of EMIC waves: Van Allen Probe observations, J. Geophys. Res. Space Physics, 120, 4400–4408, doi:10.1002/2015JA021089.

Wygant J.R. et al. (2013) The Electric Field and Waves Instruments on the Radiation Belt Storm Probes Mission. In: Fox N., Burch J.L. (eds) The Van Allen Probes Mission. Springer, Boston, MA

Xiao, F., Q. Zong, Y. Wang, Z. He, Z. Su, C. Yang, and Q. Zhou (2014), Generation of proton aurora by magnetosonic waves, Sci. Rep., 4, 5190, doi:10.1038/srep05190.

Yu, X., Z. Yuan, D. Wang, H. Li, S. Huang, Z. Wang, Q. Zheng, M. Zhou, C. A. Kletzing, and J. R. Wygant (2015), In situ observations of EMIC waves in O+ band by the Van Allen Probe A, Geophys. Res. Lett., 42, 1312–1317, doi:10.1002/ 2015GL063250

Yuan, Z., X. Yu, , S. Huang, D. Wang, and H. O. Funsten (2017) In situ observations of magnetosonic waves modulated by background plasma density, *Geophys. Res. Lett., 44(15), 7628-7633,* doi:10.1002/2017GL074681

Yuan, Z., Yu, X., Huang, S., Qiao, Z., Yao, F., & Funsten, H. O. (2018). Cold ion heating by magnetosonic waves in a density cavity of the plasmasphere. *Journal of Geophysical Research: Space Physics*, 123, 1242–1250. https://doi.org/10.1002/2017JA024919

Zhou, Q., et al. (2014), Excitation of nightside magnetosonic waves observed by Van Allen Probes, *Journal of Geophysical Research: Space Physics*, 119, 9125-9133, doi:10.1002/2014JA020481

Figure 1. Geomagnetic activity for June 23-24, 2013 (WDC, Kyoto). From top to bottom: Kp index (shown along top axis), AU and AL indices, ASY-D and ASY-H indices and SYM-H index. Van Allen Probe A observes magnetosonic waves and ion heating between 05:30-06:30 UT on June 24th . The rectangular shape marks the heating interval.

Figure 2. Van Allen Probe A observations on June 24th, 2013 between 3:00 UT and 9:00 UT. **(a-b)** The electric and magnetic field spectral intensities observed by Electric and Magnetic Field Instrument Suite and Integrated Science Instrument. **(c)** The wave normal angle (WNA), the angle between the wave vector $\hat{k}$ and the ambient magnetic field. **(d)** The wave ellipticity, the degree of elliptical polarization. The white lines on each panel denote the lower hybrid resonance frequency and the local gyrofrequency for hydrogen. Two magnetosonic waves are identified during the time intervals between 5:38 UT and 5:52 UT and between 6:06 UT and 6:14 UT.

Figure 3. Van Allen Probe A observations on June 24th, 2013 between 5:30 UT and 6:30 UT. **(a)** The electron density determined by EMFISIS through tracking the upper hybrid resonance

frequency. **(b)** The electric field spectral intensity observed by EMFISIS. The top white line represents the lower hybrid resonance frequency and the bottom white line represents the local H+ gyrofrequency. **(c, e, g)** HOPE mass spectrometer omnidirectional fluxes for H+, He+, and O+ respectively. The black dashed line in **(c)** represents the proton ring energy, E_R. The white line in (c) represents the Alfvenic energy, E_A. **(d, f)** HOPE pitch angle distributions for H+ and He+ ions binned at energies from 21 eV to 215 eV. **(h)** HOPE pitch angle distributions for O+ ions binned at energies from 16 eV to 173 eV.

Figure 4. Van Allen Probe A HOPE observations on June 24th, 2013 between 5:30 and 6:30 UT of relative and absolute partial ion number densities for energies 30 eV and up. **(a)** The ratio of warm n(H+)/n (black), warm n(He+)/n (green), warm n(O+)/n (red). **(b)** warm H+ partial number density n(H+) (black), warm He+ partial number density n(He+) (green), warm O+ partial number density n(O+) (red). Probe A observes a density channel during the interval 5:38 UT to 5:52 UT and during the interval 6:05 UT to 6:15 UT. Rectangular areas mark O+ heating intervals.

Figure 5. Fourier transformed EMFISIS magnetic field waveforms captured for 0.5 seconds with a sampling rate of 35,000 samples/second on June 24th, 2013 at 5:49 UT, during the intense O+ heating interval in the first density channel. The local proton gyrofrequency is calculated by magnetometer data and is 11.2 Hz at this time. **(a)** The total magnetic field wave power as a

function of frequency is plotted on a log scale between 0 Hz and 450 Hz with local proton gyroharmonics shown by vertical grey lines. The frequency range of the magnetosonic wave emission (between ~200 Hz and ~380 Hz) is shown with two yellow vertical lines. **(b)** The total magnetic field wave power of the magnetosonic wave emission as a function of frequency is plotted on a linear scale between 180 Hz and 380 Hz. The local proton gyroharmonics are plotted with grey lines and the local helium gyroharmonics (1/4 the local proton gyroharmonics) are shown with green dashed lines.

Figure 6. Fourier transformed Van Allen Probe A EMFISIS waveforms captured for 0.5 seconds with a sampling rate of 35,000 samples/second on June 24th, 2013 for the case of the second density channel. The magnetic field power spectral densities are averaged over time and plotted as a function of frequency. The local proton gyroharmonics are shown by solid grey lines. The frequency range for the magnetosonic wave emission is marked by two yellow lines. **(a)** Eight waveforms FFT'd and averaged over 6:06 UT and 6:10 UT, plotted on a log scale between 50 Hz and 300 Hz. The local proton gyrofrequency is 7.4 Hz. **(b)** Same as (a) except plotted on a linear scale between 150 Hz and 300 Hz. **(c)** Eight waveforms FFT'd and averaged over 6:10 UT and 6:14 UT, plotted on a log scale between 50 Hz and 300 Hz. The local proton gyrofrequency is 6.85 Hz. **(d)** Same as (c) except plotted on a linear scale between 150 Hz and 300 Hz.

Figure 7. Geomagnetic activity for August 13-14, 2013 (WDC, Kyoto). From top to bottom: Kp index (shown across the top axis, AU and AL indices, ASY-D and ASY-H indices and SYM-H index. Van Allen Probe A observes magnetosonic waves and heavy ion heating between 11:50-12:30 UT on August 14th . The rectangle area marks the heating interval.

Figure 8. Van Allen Probe A observations on August 14th, 2013 between 11:30 UT and 12:30 UT. **(a-b)** The magnetic and electric field spectral intensities observed by Electric and Magnetic Field Instrument Suite and Integrated Science Instrument. **(c)** The wave normal angle (WNA), the angle between the wave vector $\hat{k}$ and the ambient magnetic field. **(d)** The wave ellipticity, the degree of elliptical polarization. The white lines on each panel denote the lower hybrid resonance frequency and the local gyrofrequency for hydrogen.

Figure 9. Van Allen Probe A observations on August 14th, 2013 between 11:30 UT and 12:30 UT. **(a)** The electron density determined by EMFISIS through tracking the upper hybrid resonance frequency. **(b)** The electric field spectral intensity observed by EMFISIS. The top white line represents the lower hybrid resonance frequency and the bottom white line represents the proton local gyrofrequency. **(c, e, g)** HOPE mass spectrometer omnidirectional fluxes for H+, He+, and O+ respectively. The white line in (c) represents the Alfvenic energy, E_A. The dashed black line in **(c)** represents the proton ring energy, E_R. **(d, f, h)** HOPE mass spectrometer pitch angle distributions for H+, He+, and O+ sampled at energies from 13 eV to 156 eV.

Figure 10. Van Allen Probe A observations on August 14th, 2013 between 11:30 and 12:30 UT of relative and absolute partial ion number densities for warm plasma (energies 30 eV and up). **(a)** The ratio of warm n(H+)/n (black), warm n(He+)/n (green), warm n(O+)/n (red). **(b)** warm H+ partial number density (black), warm He+ partial number density (green), warm O+ partial number density (red). Probe A observes a density channel and oxygen ion heating primarily during the interval 11:54 UT to 12:01 UT. The rectangular area marks O+ heating interval.

Figure 11. Van Allen Probe A EMFISIS waveforms captured for 5.968 seconds with a sampling rate of 35,000 samples/second on August 14th, 2013 over the time interval 11:57 UT to 11:59 UT, within the O+ heating event. The average local proton gyrofrequency is 9.72 Hz. The local proton gyroharmonics are shown with grey lines. The local helium gyroharmonics are shown with green dashed lines and the local oxygen gyroharmonics are shown with red dashed lines. **(a)** Nine total magnetic field waveforms are transformed and time-averaged to show the magnetic field power spectrum centered at 11:58 UT as a function of frequency between 0 and 300 Hz. **(b)** Same as (a) except between 70 Hz and 100 Hz. **(c)** Same as (a) except between 120 Hz and 150 Hz.

Event	Type of MS wave process for oxygen

	gyroharmonics
June 24th, 2013 – First Density Channel	-wave propagates from region of low B_f to region of high B_f, while retaining harmonic structure of source conditions -mixture of multiple waves
June 24th, 2013 – Second Density Channel	-wave propagates from region of low B_f to region of high B_f, while retaining harmonic structure of source conditions -mixture of multiple waves
August 14th, 2013 – Third Density Channel	-wave propagates from region of low B_f to region of high B_f, while retaining harmonic structure of source conditions -mixture of multiple waves -wave structure transforms from discrete to continuous

Table 1. For each oxygen heating event presented in this paper, we suggest different ways that the magnetosonic wave could have oxygen gyroharmonics.

Figure 12. (a) Drawing of the plasmasphere conditions during June 24, 2013 between 5:30 UT and 6:30 UT. The Van Allen Probe A spacecraft trajectory between 17 and 19 MLT is plotted with a red arrow. The spacecraft trajectory crosses two density channels over the time interval. **(b)** Drawing of the plasmasphere conditions during August 14th, 2013 between 11:30 UT and 12:30 UT. The spacecraft trajectory between 15 and 17 MLT is plotted with a red arrow. Probe A crosses a density channel and thin plume. The drawing is modified from Figure 6 in Sandel et al., 2003.

Figure 13. 8192-point Fourier transform of the Van Allen Probe A EMFISIS high resolution magnetometer data captured at 64 samples/s of the By magnetic field component in GSM coordinates. **(a)** 5:30-6:30 UT June 24th, 2013 – the time interval corresponding to the first O+ heating event in this study. Each density channel with O+ heating is marked by a yellow rectangle. **(b)** 11:30-12:30 UT August 14th, 2013 – the time interval corresponding to the second O+ heating event in this study. The O+ heating event is marked by a yellow rectangle. **(c)** 17:00-18:00 UT October 8th, 2012 – the time interval for the EMIC wave event presented in Yu et al., (2015). The white lines in all three panels represent the local helium gyrofrequency (top) and the local oxygen gyrofrequency (bottom).

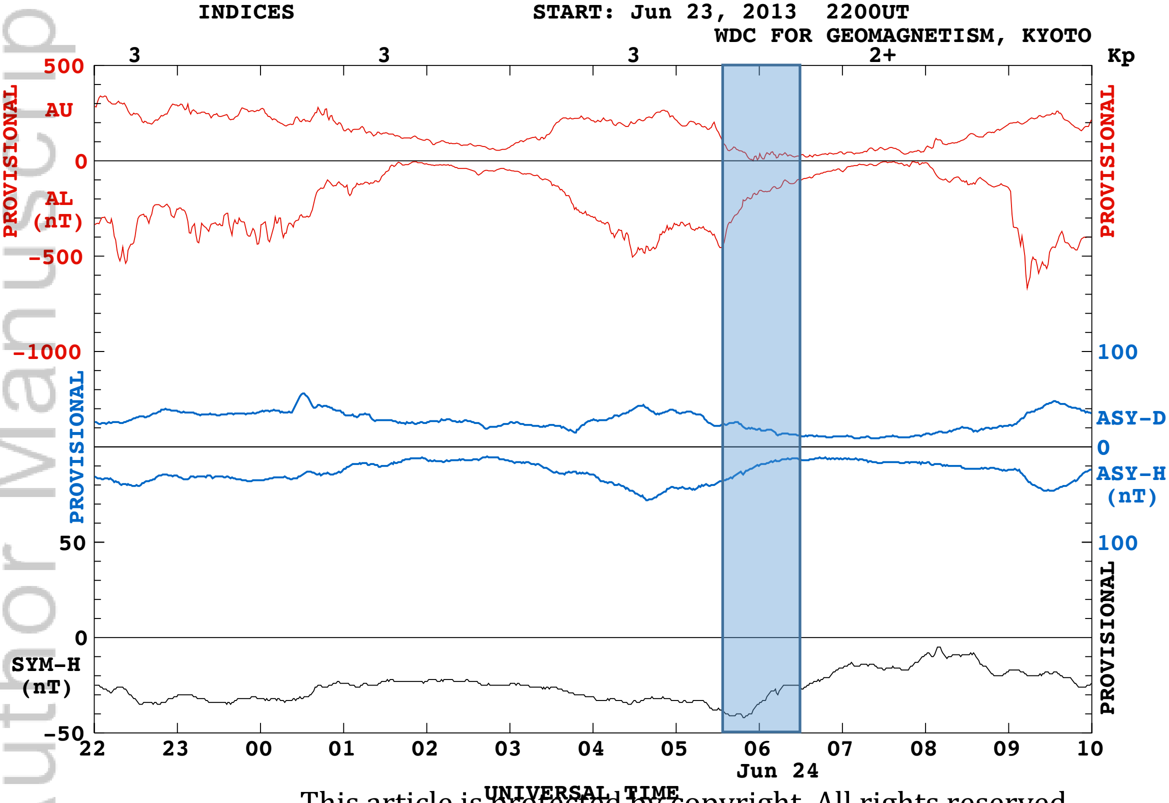
INDICES
START: Jun 23, 2013 2200UT
WDC FOR GEOMAGNETISM, KYOTO
Kp
3
3
3
2+
500
AU
0
AL
(nT)
-500
-1000
PROVISIONAL
PROVISIONAL
100
ASY-D
0
ASY-H
(nT)
100
PROVISIONAL
50
0
SYM-H
(nT)
-50
PROVISIONAL
22
23
00
01
02
03
04
05
06
07
08
09
10
Jun 24
UNIVERSAL TIME

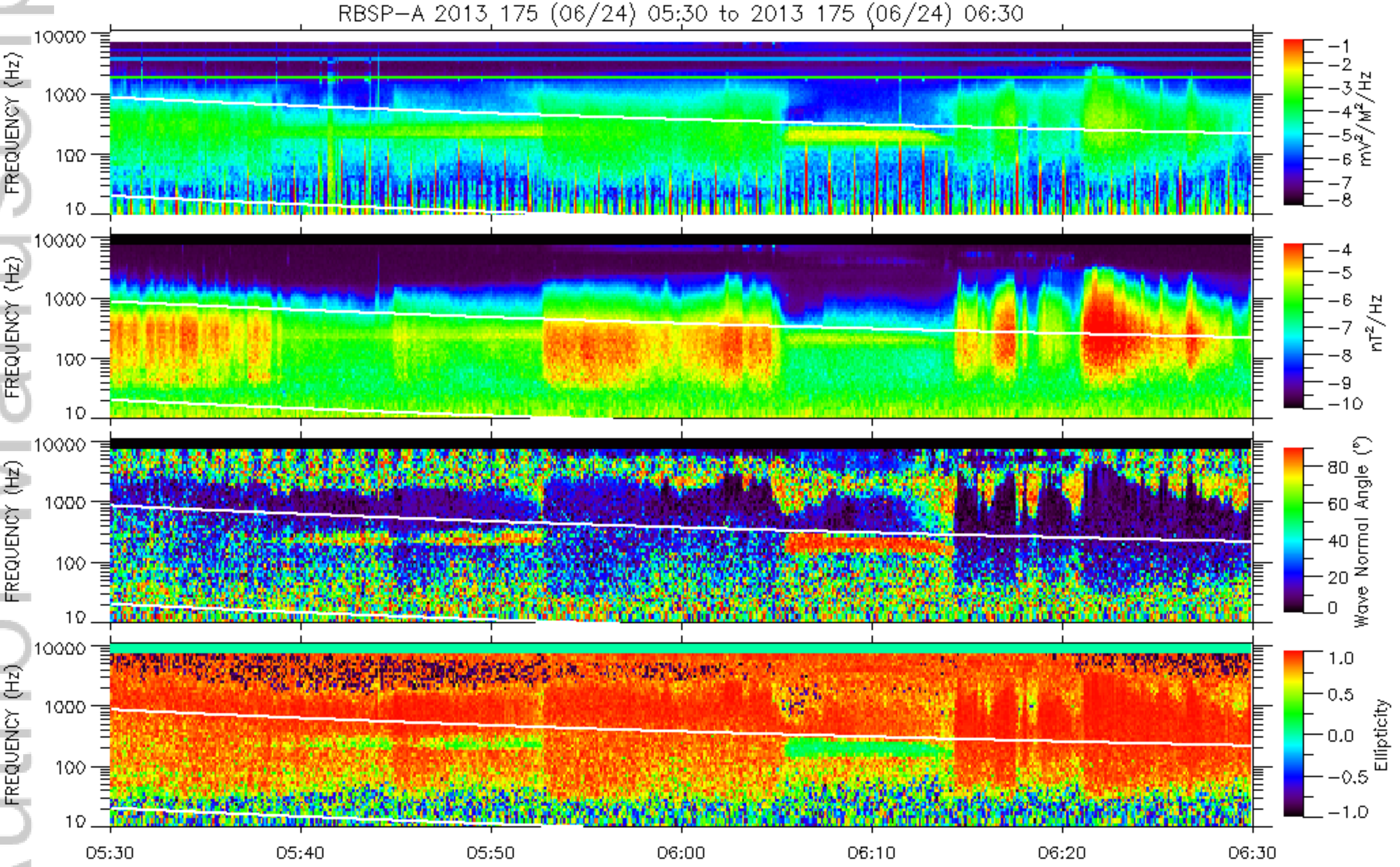
RBSP-A 2013 175 (06/24) 05:30 to 2013 175 (06/24) 06:30
FREQUENCY (Hz)
10000
1000
100
10
mV²/M²/Hz
-1
-2
-3
-4
-5
-6
-7
-8
nT²/Hz
-4
-5
-6
-7
-8
-9
-10
Wave Normal Angle (°)
80
60
40
20
0
Ellipticity
1.0
0.5
0.0
-0.5
-1.0
05:30
05:40
05:50
06:00
06:10
06:20
06:30

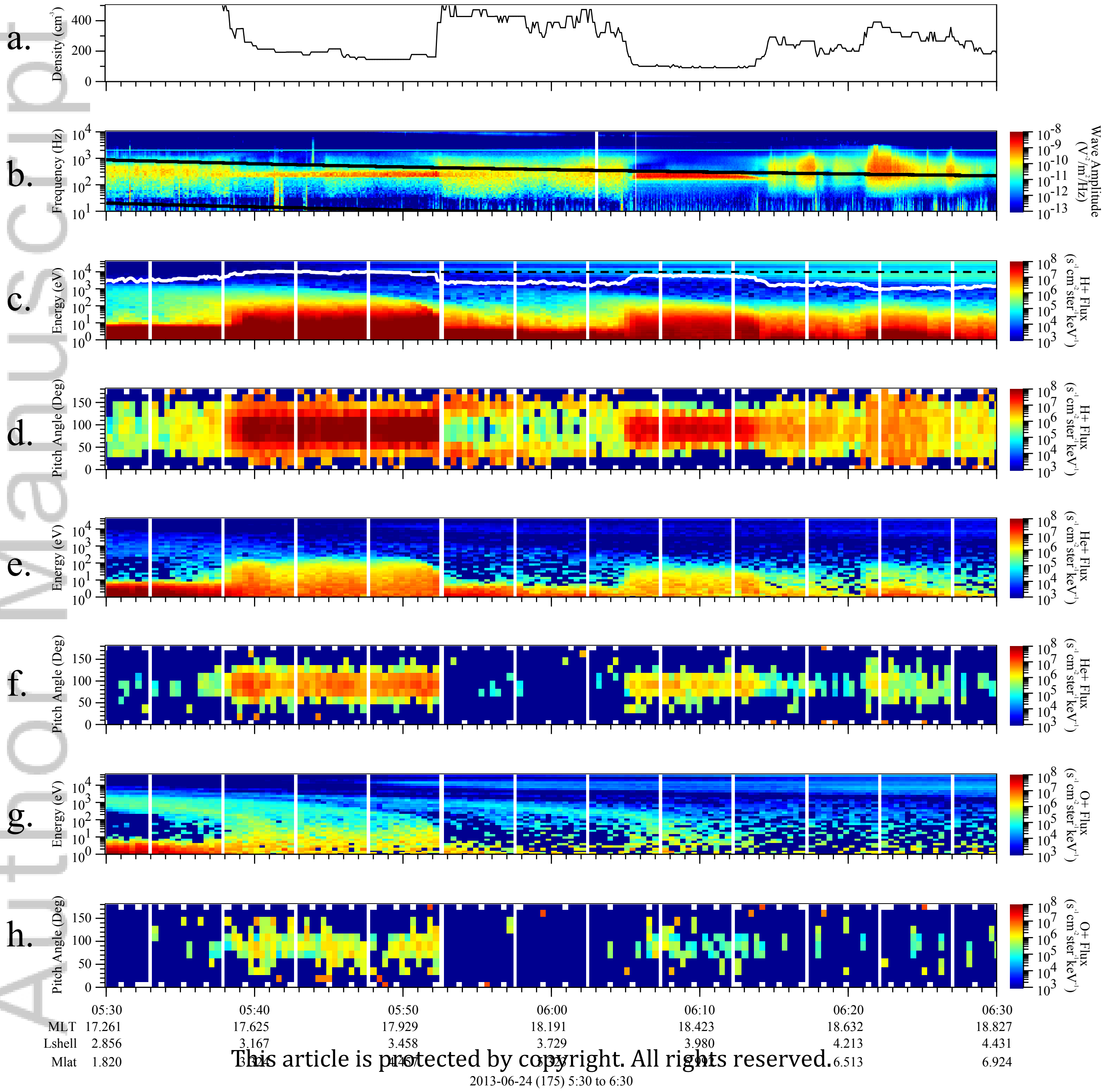
a.
Density (cm⁻³)
400
200
0
b.
Frequency (Hz)
10^4
10^3
10^2
10^1
Wave Amplitude (V²/m²/Hz)
10^-8
10^-9
10^-10
10^-11
10^-12
10^-13
c.
Energy (eV)
H+ Flux (s⁻¹ cm⁻² ster⁻¹ keV⁻¹)
d.
Pitch Angle (Deg)
150
100
50
0
H+ Flux (s⁻¹ cm⁻² ster⁻¹ keV⁻¹)
e.
Energy (eV)
He+ Flux (s⁻¹ cm⁻² ster⁻¹ keV⁻¹)
f.
Pitch Angle (Deg)
He+ Flux (s⁻¹ cm⁻² ster⁻¹ keV⁻¹)
g.
Energy (eV)
O+ Flux (s⁻¹ cm⁻² ster⁻¹ keV⁻¹)
h.
Pitch Angle (Deg)
O+ Flux (s⁻¹ cm⁻² ster⁻¹ keV⁻¹)
10^8
10^7
10^6
10^5
10^4
10^3
05:30
05:40
05:50
06:00
06:10
06:20
06:30
MLT 17.261 17.625 17.929 18.191 18.423 18.632 18.827
Lshell 2.856 3.167 3.458 3.729 3.980 4.213 4.431
Mlat 1.820 6.513 6.924
2013-06-24 (175) 5:30 to 6:30


a.
Ion Composition Ratio
1.0
0.8
0.6
0.4
0.2
0.0
H+
O+
He+
05:30
2013-06-24
05:40
05:50
06:00
06:10
06:20
06:30
b.
Ion partial number density (cm⁻³)
10¹
10⁰
10⁻¹
10⁻²
10⁻³
H+
O+
He+
05:30
2013-06-24
05:40
05:50
06:00
06:10
06:20
06:30

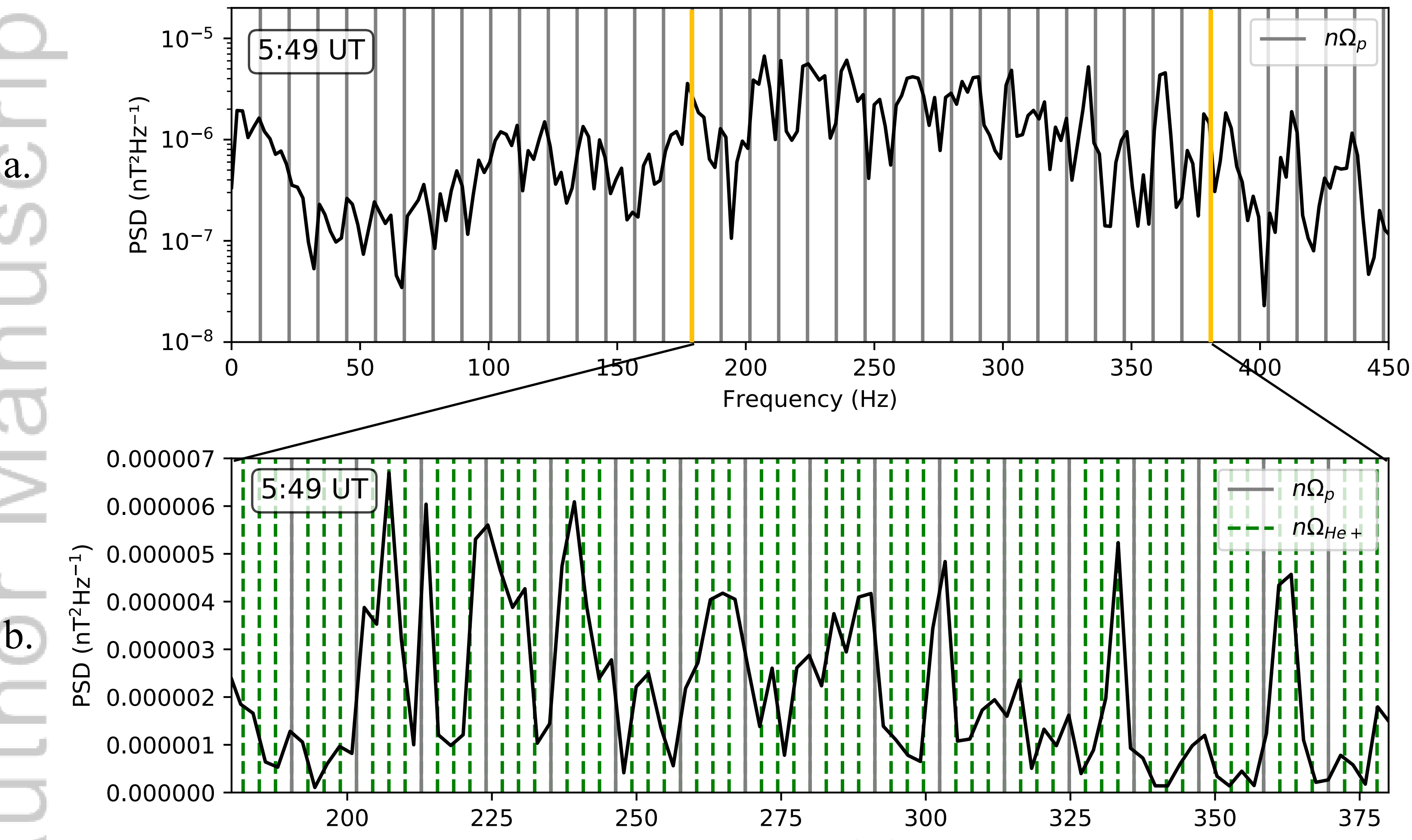
a.
5:49 UT
$n\Omega_p$
PSD (nT^{2}Hz^{-1})
10^{-5}
10^{-6}
10^{-7}
10^{-8}
0
50
100
150
200
250
300
350
400
450
Frequency (Hz)
b.
5:49 UT
$n\Omega_p$
$n\Omega_{He+}$
PSD (nT^{2}Hz^{-1})
0.000007
0.000006
0.000005
0.000004
0.000003
0.000002
0.000001
0.000000
200
225
250
275
300
325
350
375
Frequency (Hz)

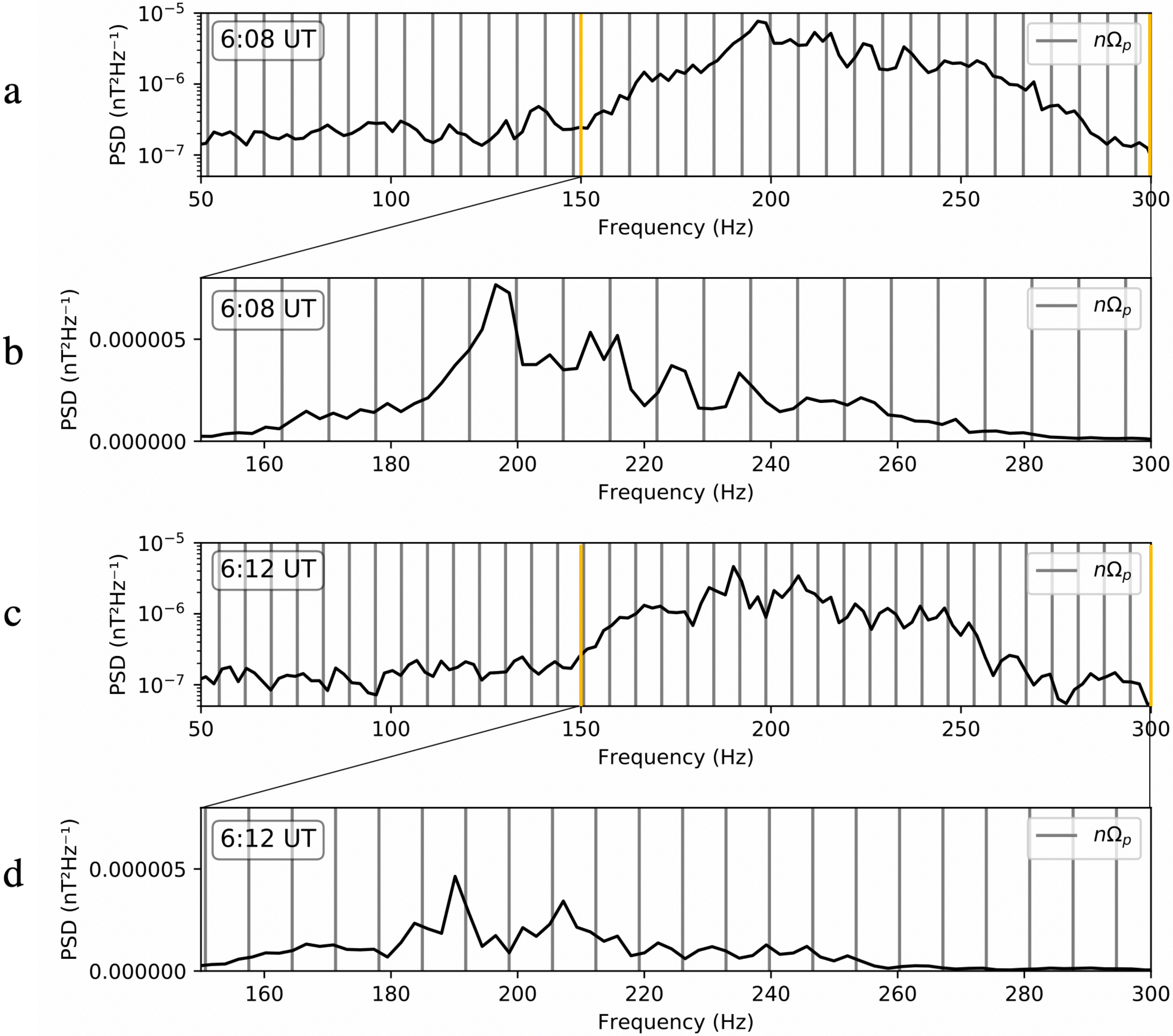
a
6:08 UT
$n\Omega_p$
PSD (nT²Hz⁻¹)
10^{-5}
10^{-6}
10^{-7}
50
100
150
200
250
300
Frequency (Hz)
b
6:08 UT
$n\Omega_p$
PSD (nT²Hz⁻¹)
0.000005
0.000000
160
180
200
220
240
260
280
300
Frequency (Hz)
c
6:12 UT
$n\Omega_p$
PSD (nT²Hz⁻¹)
10^{-5}
10^{-6}
10^{-7}
50
100
150
200
250
300
Frequency (Hz)
d
6:12 UT
$n\Omega_p$
PSD (nT²Hz⁻¹)
0.000005
0.000000
160
180
200
220
240
260
280
300
Frequency (Hz)

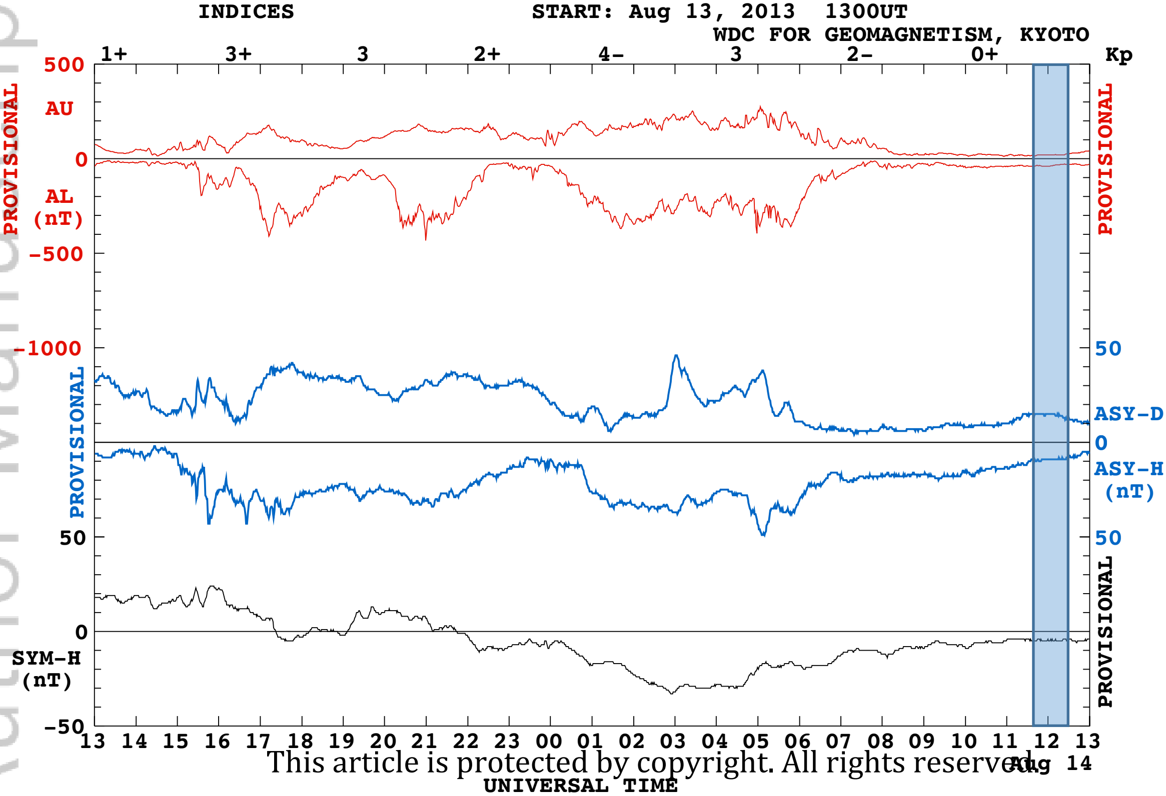
INDICES
START: Aug 13, 2013 1300UT
WDC FOR GEOMAGNETISM, KYOTO
Kp
1+
3+
3
2+
4−
3
2−
0+
PROVISIONAL
AU
AL
(nT)
500
0
−500
−1000
PROVISIONAL
50
ASY-D
0
ASY-H
(nT)
50
PROVISIONAL
SYM-H
(nT)
50
0
−50
13
14
15
16
17
18
19
20
21
22
23
00
01
02
03
04
05
06
07
08
09
10
11
12
13
Aug 14
UNIVERSAL TIME

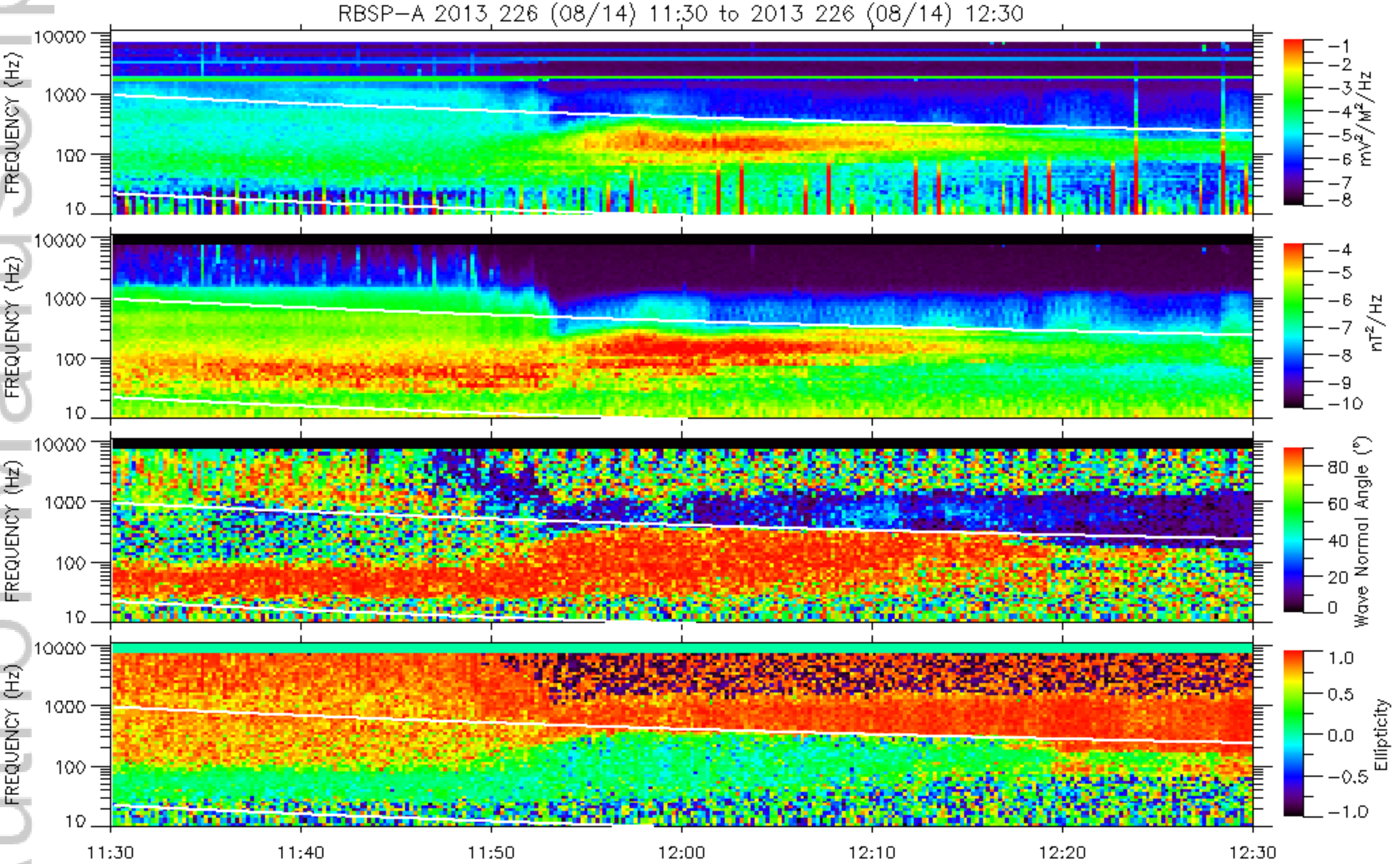
RBSP–A 2013 226 (08/14) 11:30 to 2013 226 (08/14) 12:30
FREQUENCY (Hz)
10000
1000
100
10
mV²/M²/Hz
−1
−2
−3
−4
−5
−6
−7
−8
nT²/Hz
−4
−5
−6
−7
−8
−9
−10
Wave Normal Angle (°)
80
60
40
20
0
Ellipticity
1.0
0.5
0.0
−0.5
−1.0
11:30
11:40
11:50
12:00
12:10
12:20
12:30

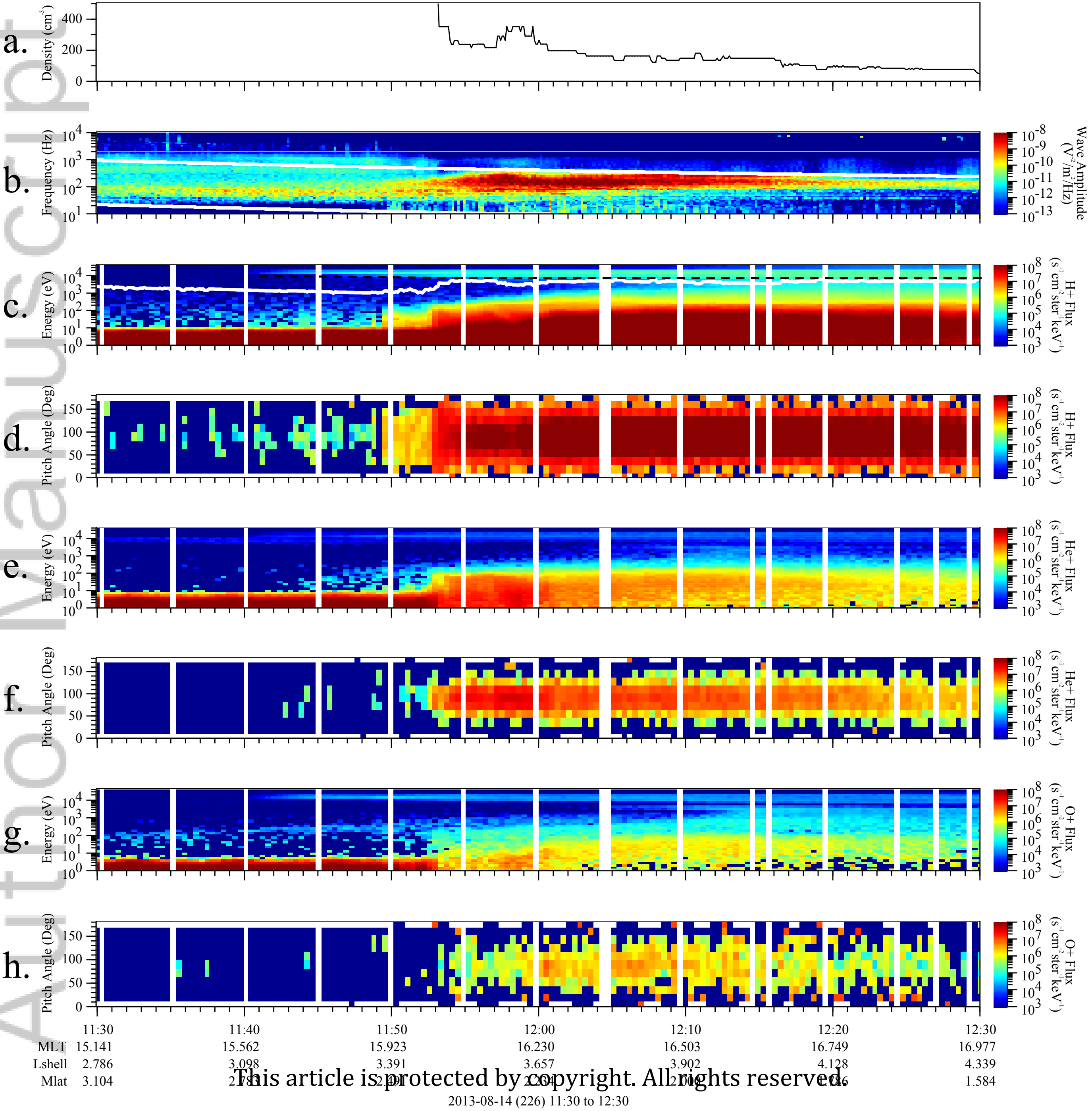
a.
Density (cm⁻³)
400
200
0
b.
Frequency (Hz)
10⁴
10³
10²
10¹
Wave Amplitude (V²/m²/Hz)
10⁻⁸ 10⁻⁹ 10⁻¹⁰ 10⁻¹¹ 10⁻¹² 10⁻¹³
c.
Energy (eV)
H+ Flux (s⁻¹ cm⁻² ster⁻¹ keV⁻¹)
d.
Pitch Angle (Deg)
150
100
50
0
H+ Flux (s⁻¹ cm⁻² ster⁻¹ keV⁻¹)
e.
Energy (eV)
He+ Flux (s⁻¹ cm⁻² ster⁻¹ keV⁻¹)
f.
Pitch Angle (Deg)
He+ Flux (s⁻¹ cm⁻² ster⁻¹ keV⁻¹)
g.
Energy (eV)
O+ Flux (s⁻¹ cm⁻² ster⁻¹ keV⁻¹)
h.
Pitch Angle (Deg)
O+ Flux (s⁻¹ cm⁻² ster⁻¹ keV⁻¹)
10⁸ 10⁷ 10⁶ 10⁵ 10⁴ 10³
11:30 11:40 11:50 12:00 12:10 12:20 12:30
MLT 15.141 15.562 15.923 16.230 16.503 16.749 16.977
Lshell 2.786 3.098 3.391 3.657 3.902 4.128 4.339
Mlat 3.104 1.584
2013-08-14 (226) 11:30 to 12:30

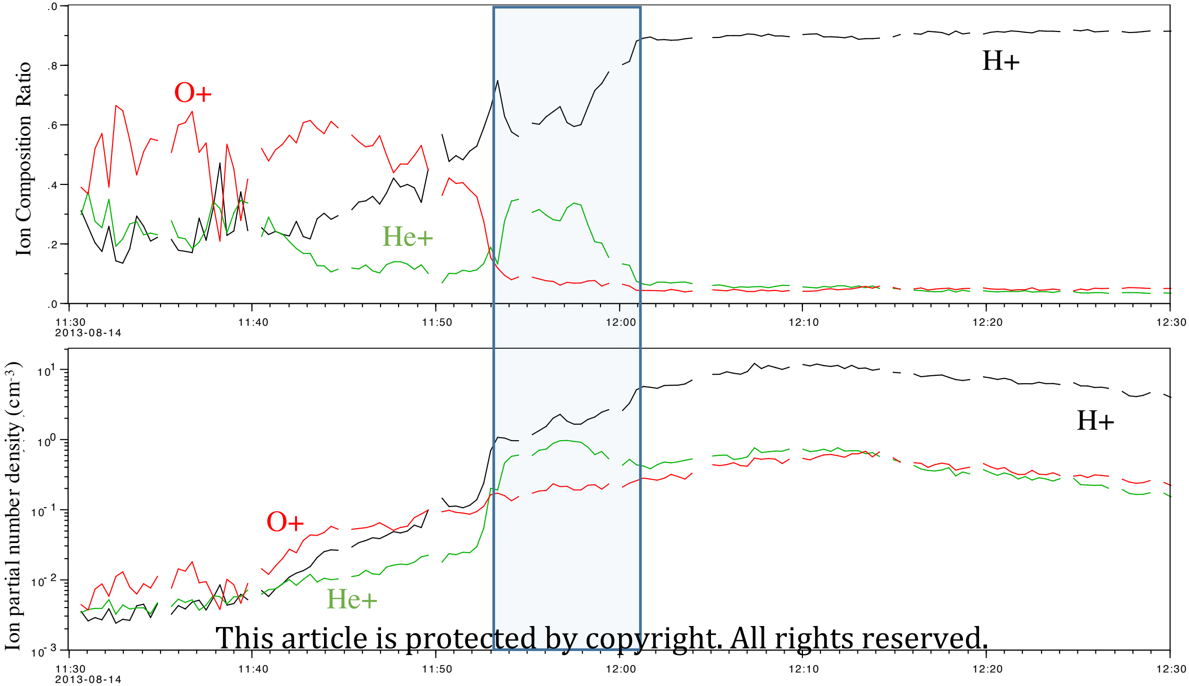
a.
Ion Composition Ratio
.0
.8
.6
.4
.2
.0
O+
He+
H+
11:30
2013-08-14
11:40
11:50
12:00
12:10
12:20
12:30
b.
Ion partial number density (cm^{-3})
10^{1}
10^{0}
10^{-1}
10^{-2}
10^{-3}
O+
He+
H+
11:30
2013-08-14
11:40
11:50
12:00
12:10
12:20
12:30

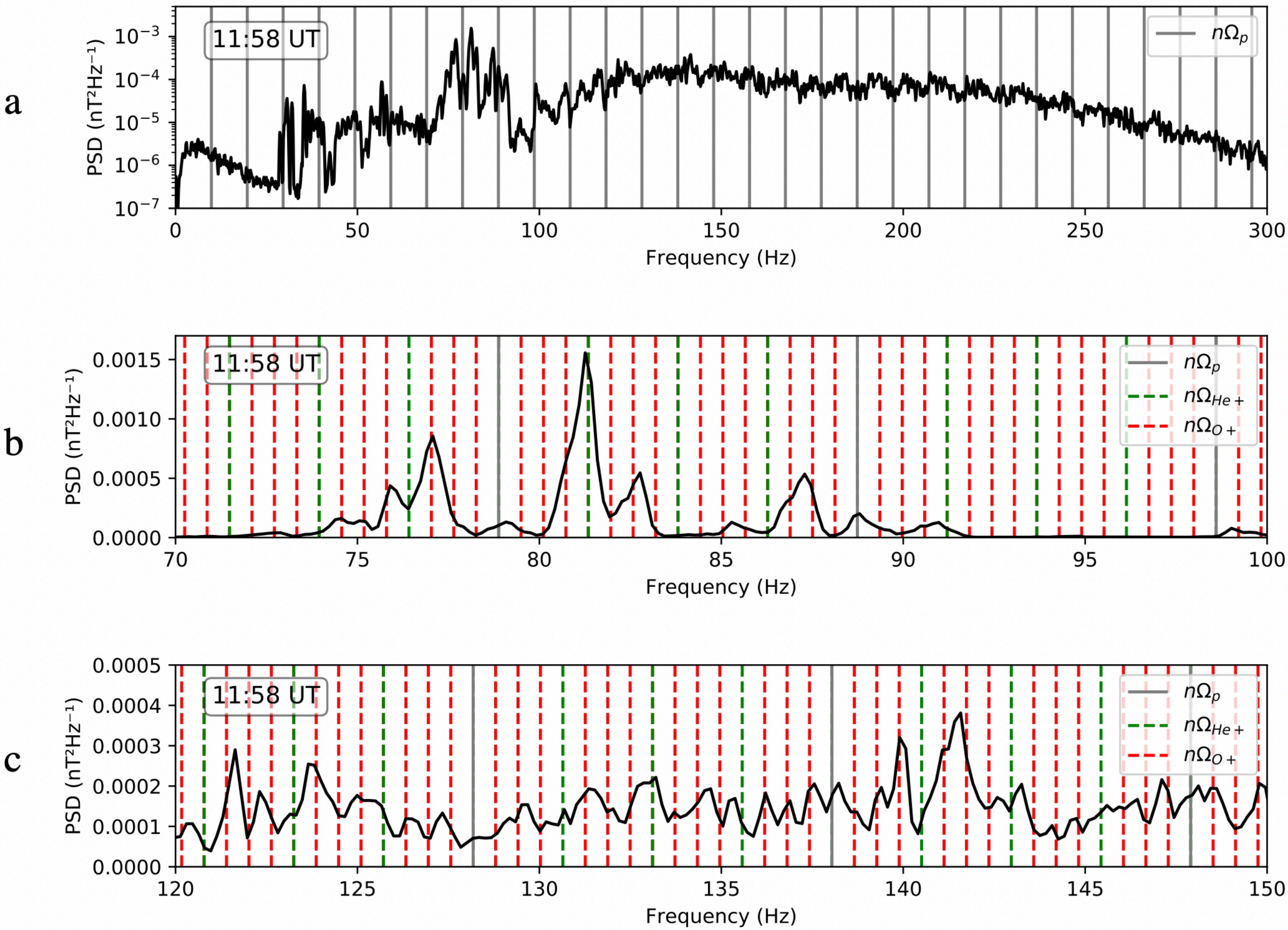
a
11:58 UT
$n\Omega_p$
PSD (nT²Hz⁻¹)
10^{-3}
10^{-4}
10^{-5}
10^{-6}
10^{-7}
0
50
100
150
200
250
300
Frequency (Hz)
b
11:58 UT
$n\Omega_p$
$n\Omega_{He+}$
$n\Omega_{O+}$
PSD (nT²Hz⁻¹)
0.0015
0.0010
0.0005
0.0000
70
75
80
85
90
95
100
Frequency (Hz)
c
11:58 UT
$n\Omega_p$
$n\Omega_{He+}$
$n\Omega_{O+}$
PSD (nT²Hz⁻¹)
0.0005
0.0004
0.0003
0.0002
0.0001
0.0000
120
125
130
135
140
145
150
Frequency (Hz)

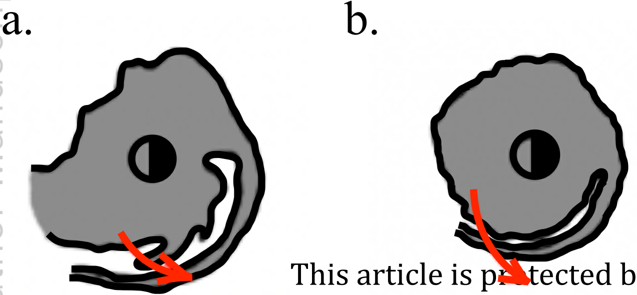
a.
b.

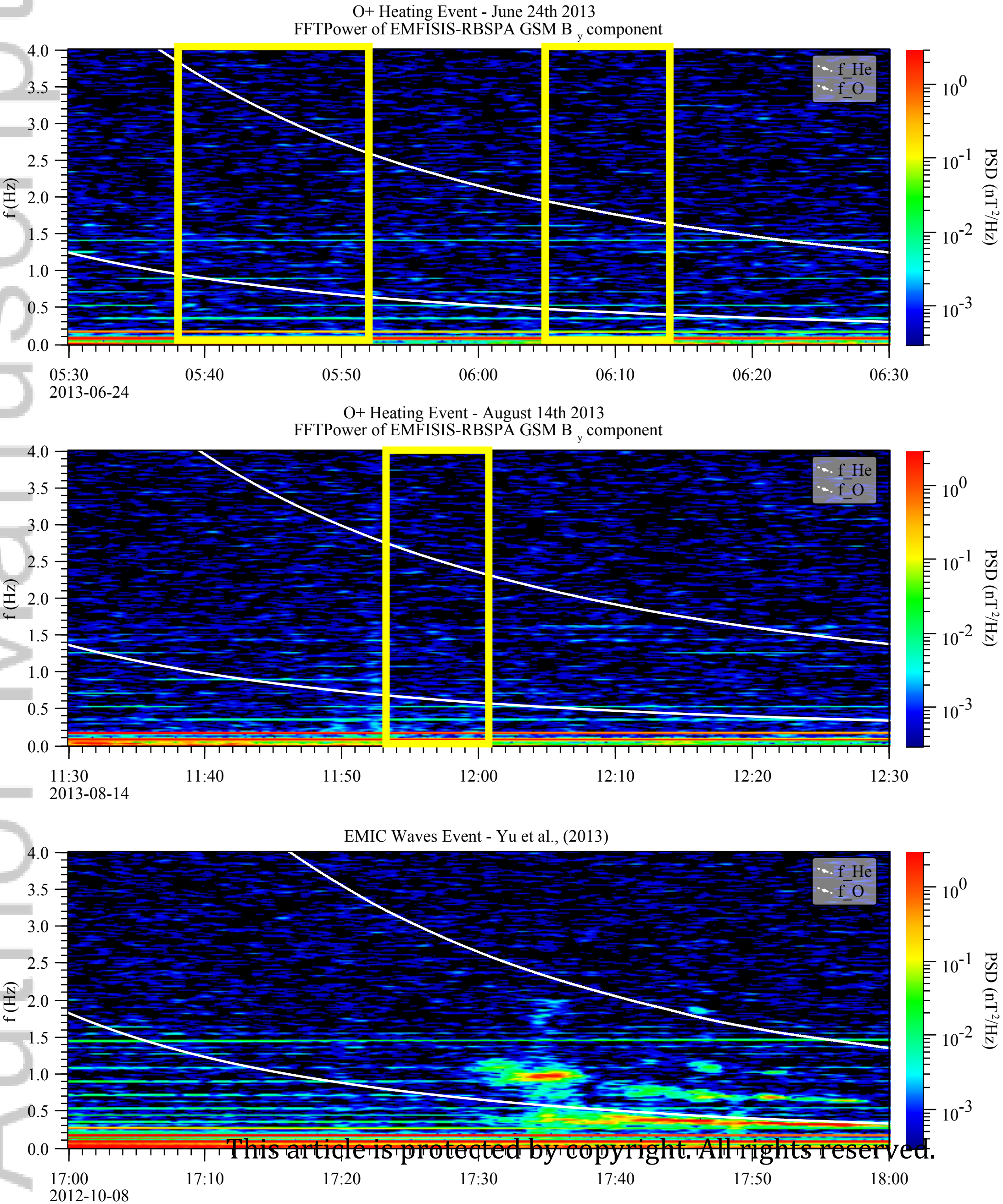
O+ Heating Event - June 24th 2013
FFTPower of EMFISIS-RBSPA GSM B y component
f (Hz)
4.0
3.5
3.0
2.5
2.0
1.5
1.0
0.5
0.0
f_He
f_O
10^0
10^{-1}
10^{-2}
10^{-3}
PSD (nT^2/Hz)
05:30
2013-06-24
05:40
05:50
06:00
06:10
06:20
06:30
O+ Heating Event - August 14th 2013
FFTPower of EMFISIS-RBSPA GSM B y component
f (Hz)
4.0
3.5
3.0
2.5
2.0
1.5
1.0
0.5
0.0
f_He
f_O
10^0
10^{-1}
10^{-2}
10^{-3}
PSD (nT^2/Hz)
11:30
2013-08-14
11:40
11:50
12:00
12:10
12:20
12:30
EMIC Waves Event - Yu et al., (2013)
f (Hz)
4.0
3.5
3.0
2.5
2.0
1.5
1.0
0.5
0.0
f_He
f_O
10^0
10^{-1}
10^{-2}
10^{-3}
PSD (nT^2/Hz)
17:00
2012-10-08
17:10
17:20
17:30
17:40
17:50
18:00